Consequences of giant impacts in early Mars: Core merging and Martian dynamo evolution

Julien Monteux, Jafar Arkani-Hamed

AGU PUBLICATIONS

JGR

Journal of Geophysical Research: Planets

RESEARCH ARTICLE
10.1002/2013JE004587

Key Points:
- Following a giant impact, the impact parameters govern the merging temperature
- For plausible viscosity contrasts the merging time occurs in less than 1 kyr
- Core merging only delays the re-initiation of the dynamo for a very short time

Correspondence to:
J. Monteux,
julien.monteux@univ-nantes.fr

Citation:
Monteux, J., and J. Arkani-Hamed (2014), Consequences of giant impacts in early Mars: Core merging and Martian dynamo evolution, *J. Geophys. Res. Planets*, *119*, doi:10.1002/2013JE004587.

Received 28 NOV 2013
Accepted 29 JAN 2014
Accepted article online 6 FEB 2014

Consequences of giant impacts in early Mars: Core merging and Martian dynamo evolution

Julien Monteux[1] and Jafar Arkani-Hamed[2]

[1]Laboratoire de Planétologie et de Géodynamique, Université de Nantes, Nantes, France, [2]Department of Physics, University of Toronto, Toronto, Ontario, Canada

Abstract A giant impact is an increasingly popular explanation for the formation of the northern lowland on Mars. It is plausible that at the impact time both Mars and the impactor were differentiated with solid silicate mantles and liquid iron cores. Such a large impact likely resulted in merging of the cores of both bodies, a process which will have implications on the thermal state of the planet. We model the evolution of the Martian mantle following a giant impact and characterize the thermochemical consequences of the sinking of an impactor's core as a single diapir. The impact heating and the viscous heating induced during the core merging may affect the early thermal state of Mars during several tens of million years. Our results show that large viscosity contrasts between the impactor's core and the surrounding mantle silicates can reduce the duration of the merging down to 1 kyr but do not modify the merging temperature. When the viscosity contrast between the diapir and the surrounding silicates is larger than a factor of 1000, the descent of the diapir can lead to some entrainment of the relatively shallow silicates to deepest regions close to the core-mantle boundary. Finally, the direct impact heating of Martian core leads to thermal stratification of the core and kills the core dynamo. It takes on the order of 150–200 Myr to reinitiate a strong dynamo anew. The merging of the impactor's core with the Martian core only delays the reinitiation of the dynamo for a very short time.

1. Introduction

Giant impacts were common in the later stage of accretion of terrestrial planets. The Earth is likely formed by accretion of a few dozen moons to Mars-size planetary embryos (see the review by *Chambers* [2004]). A Mars-size impact on Earth may have resulted in the formation of the Moon [*Hartmann and Davis*, 1975; *Cameron and Benz*, 1991; *Canup*, 2004]. An oblique collision of a large body with a mass about one sixth of the Mercury's has likely stripped away a significant part of Mercury's mantle [*Smith*, 1979; *Benz et al*., 1988]. As an alternative to endogenic formation models [e.g., *Zhong and Zuber*, 2001; *Reese and Solomatov*, 2006], an 800–1300 km size impact has been proposed to explain the formation of northern lowland of Mars [*Wilhelms and Squyres*, 1984; *Nimmo et al*., 2008; *Andrews-Hanna et al*., 2008; *Marinova et al*., 2008], and the lunar farside highlands were likely formed by accretion of a companion moon [*Jutzi and Asphaug*, 2011].

Part of an impactor may be retained by the planet, depending on the impact angle, impact velocity and the impactor to planet mass ratio. The accretion efficiency is close to 1 for impacts occurring at low velocities (i.e., the impact velocity $v_{imp} <$ twice the escape velocity of the planet v_{esc}) with impact angles of ~45° or less relative to the local vertical direction, whereas for impacts occurring at higher velocities (i.e., $v_{imp} > 2v_{esc}$) and at higher impact angles the efficiency is negligible [*Asphaug*, 2010]. The impact-induced shock wave propagation heats the planet and results in a large thermal anomaly buried deep in the mantle of the planet with a volume comparable to the volume of the impactor [e.g., *Tonks and Melosh*, 1993; *Pierazzo et al*., 1997; *Arkani-Hamed*, 2005; *Monteux et al*., 2007; *Arkani-Hamed and Ghods*, 2011]. This thermal energy added to the preimpact temperature of a planet may result in melting and iron-silicate segregation in the mantle.

Recent studies have explored the effects of large impacts on the Martian mantle dynamics [e.g., *Watters et al*., 2009; *Ghods and Arkani-Hamed*, 2011; *Roberts and Arkani-Hamed*, 2012] and on the cessation of dynamo action [e.g., *Roberts et al*., 2009; *Arkani-Hamed and Olson*, 2010a, 2010b; *Arkani-Hamed*, 2012]. At the time of a giant impact, both Mars and the impactor were probably differentiated [*Yoshino et al*., 2003; *Neumann et al*., 2012]. It is likely that the entire impactor's iron core merged with the preexisting core of Mars. The processes involved in the merging dynamics are strongly dependent on the rheology of the impacted mantle where the iron core of the impactor sinks and on the characteristic size of the sinking core. These processes can involve sedimentation of metallic rain at the base of a magma ocean [*Rubie et al*., 2003; *Höink et al*., 2005]

followed by a large diapir, which sinks through the underlying solid mantle [*Tonks and Melosh*, 1992]. The impact heating can have severe consequences on the thermal state of the planet and on the cessation of the core dynamo [e.g., *Arkani-Hamed and Olson*, 2010a, 2010b]. Also, the hot and molten iron brought by the merging of an impactor's core can envelop the preexistent core and generate dynamo if the layer is thicker than about 30 km [*Reese and Solomatov*, 2010].

Monteux et al. [2013] investigated the dynamics and the thermal effects of the core merging by monitoring the evolution of a spherical diapir sinking through a solid mantle. The authors used some idealized models of Mars and the impact heating as first-order estimates. For example (1) the iron diapir is assumed to start as a spherical body. During the impact process, the molten iron of the impactor is mixed with the partially molten parts of the impactor's and planet's silicates. However, due to its higher density compared to the silicates, the molten iron segregates and pounds at the bottom of the partially molten zone in the mantle while conforming to the shape of the zone. Hence, the initial shape of the iron diapir is a thin spherical cap with a flat top and an almost spherical bottom, certainly far from being spherical. Because the dynamics of a sinking body is strongly affected by its shape the spherical shape assumption has significant effects on the sinking time of the diapir. (2) The impact creates a spherical isobaric zone with an almost constant temperature, and temperature decays exponentially outside this zone. By choosing the decay scaling factor of $\sim (r_o/r)^{4.4}$, where r_o and r denote the radius of the isobaric sphere and the distance from the center of the sphere, the authors severely underestimated the impact-induced temperature increase outside the isobaric core. This resulted in much colder thus higher viscosity lower mantle beneath the impact site in their temperature-dependent viscosity models, hence hampering the sinking of the iron diapir. (3) The mantle viscosity was assumed either constant (isoviscous) or temperature dependent. The mantle viscosity is actually temperature and pressure dependent, decreases with increasing temperature and increases with increasing pressure. Also the viscosity reduces substantially upon partial melting. Moreover, in reality, the rheology also depends on the strain rate and plasticity can occur [*Golabek et al*., 2009]. The latter is not taken into account here.

The aim of the present study is to monitor the thermal evolution of the Martian mantle following a giant impact and, in particular, the dynamics of the sinking iron diapir of the impactor. We relax the assumptions made by *Monteux et al*. [2013] by using more realistic models. This provides a means to assess the adverse effects of the assumptions. For example, (1) we start with the molten iron of the impactor as an almost spherical cap, numerically determined by the shape of the partially molten impact-heated region in the upper mantle of the Mars models, (2) we use a more realistic scaling law for the decay of temperature outside the isobaric zone derived on the basis of hydrocode numerical simulations of an impact [*Pierazzo et al*., 1997; *Watters et al*., 2009], and (3) we use not only constant and temperature-dependent viscosity models but also incorporate the pressure- and melt-dependent viscosity models. Furthermore, we investigate the effects of other factors such as (1) the higher viscosity contrast between the iron diapir and the surrounding mantle, (2) the higher impact velocity of 10 km/s which is within the range of impact velocities of Mars [*Neukum and Wise*, 1976] (on Mars, $v_{esc} = 5$ km/s), (3) different physical properties of Martian mantle which control the Equation Of State (EOS) for propagation of shock waves, hence the ability of the mantle to convert the energy from the impact-induced shock wave to internal heating, and (4) the influence of melting on the heat budget and mantle dynamics. In comparison with the models from *Monteux et al*. [2013], the preimpact thermal state, the postimpact thermal state, the postimpact chemical repartition of the impactor's core, and the mantle viscosity are considered more realistically. We also investigate in detail the effect of an impact on the core dynamo of Mars. This includes two aspects: (1) the direct heating of the core by the impact-induced shock wave, and (2) the impactor core merging on the Martian core. The first aspect, which is the most important factor, was not considered by *Monteux et al*. [2013], but the second aspect was also investigated by the authors.

The second section deals with the preimpact Martian model, while the third section presents the postimpact temperature and chemical repartitions. The core merging dynamics is described in the fourth section, and the results are presented in the fifth, sixth, and seventh sections. The effects of impacts on the core dynamo of Mars are investigated in the following section. The concluding remarks are relegated to the last section.

2. Preimpact Martian Model

This section describes the preimpact models of Mars considered in this study. The models are spherically symmetric with radially dependent physical parameters.

2.1. Pressure and Gravity Profiles

The Martian topographic dichotomy is one of the oldest features on Mars, formed sometime between 4.5 and 3.7 Ga [*McGill and Dimitriou*, 1990; *Frey et al.*, 2002; *Solomon et al.*, 2005]. Hence, at the time of the giant impact that might be responsible for the Martian dichotomy, both the impactor and Mars were probably differentiated. Hf/W chronology suggests that core formation happened during the first 10–30 Myr of Mars' history [*Lee and Halliday*, 1997; *Kleine et al.*, 2002; *Nimmo and Kleine*, 2007; *Dauphas and Pourmand*, 2011]. Such a rapid process involves extensive melting, which is potentially enhanced by radiogenic heating as a result of the decay of short-lived radionuclides ^{26}Al and ^{60}Fe [*Yoshino et al.*, 2003; *Neumann et al.*, 2012], impact heating [*Tonks and Melosh*, 1992; *Senshu et al.*, 2002; *Monteux et al.*, 2009], and gravitational energy conversion during the core formation resulting in metal/silicate separation [*Stevenson*, 1989; *Ricard et al.*, 2009]. The metal/silicate separation can occur via a wide range of phenomena such as percolation [*Shannon and Agee*, 1996; *Walte et al.*, 2007; *Bagdassarov et al.*, 2009; *Walte et al.*, 2011], the sedimentation of metallic rain through a magma ocean [*Rubie et al.*, 2003; *Höink et al.*, 2005] or a large diapir sinking through a solid mantle [*Tonks and Melosh*, 1992; *Monteux et al.*, 2009]. Whatever the mechanism, Mars' internal structure, characterized by a $\approx$1700 km radius liquid iron core [*Yoder et al.*, 2003], was mostly established within $\approx$10 Myr of the planet's formation [*Kleine et al.*, 2002].

Considering a simple two-layered density model, ρ_{Fe} for the core (with radius R_{core}) and ρ_{Si} for the mantle, the integration of

$$dP = -\rho g dr \tag{1}$$

leads to the following gravity and pressure profiles in the core,

$$g(r) = \frac{4}{3}\pi G \rho_{Fe} r \tag{2}$$

$$\begin{aligned} P(r) = {} & \frac{2}{3}\pi G \rho_{Fe}^2 \left(R_{core}^2 - r^2\right) + \frac{2}{3}\pi G \rho_{Si}^2 \left(R^2 - R_{core}^2\right) \\ & + \frac{4}{3}\pi G \rho_{Si} R_{core}^3 \left(\rho_{Fe} - \rho_{Si}\right)\left(\frac{1}{R_{core}} - \frac{1}{R}\right) \end{aligned} \tag{3}$$

and in the mantle,

$$g(r) = \frac{4}{3}\pi G \left(r\rho_{Si} + \frac{R_{core}^3}{r^2}\left(\rho_{Fe} - \rho_{Si}\right)\right) \tag{4}$$

$$P(r) = \frac{2}{3}\pi G \rho_{Si}^2 \left(R^2 - r^2\right) + \frac{4}{3}\pi G \rho_{Si} R_{core}^3 \left(\rho_{Fe} - \rho_{Si}\right)\left(\frac{1}{r} - \frac{1}{R}\right) \tag{5}$$

where ρ_{Fe} and ρ_{Si} are assumed constant, g is the gravitational acceleration, r is the distance to the center of the planet, and G is the gravitational constant. Figure 1 presents the density, gravity, and pressure profiles used in our models.

2.2. Temperature Field

The preimpact thermal state of Mars strongly depends on the short-lived radiogenic heating, the accretion processes and the dissipation of potential energy during the core formation [e.g., *Senshu et al.*, 2002; *Golabek et al.*, 2009; *Šrámek et al.*, 2010]. The uncertainties on the relative importance of these processes as well as the diversity of the processes involved in the core formation lead to a wide range of plausible early thermal states after the full differentiation of Mars.

The preimpact Martian temperature field is assumed only radially dependent. From the surface, the temperature increases rapidly through the top thermal boundary layer and then increases adiabatically and gradually down to the bottom thermal boundary layer, where it again increases rapidly toward the core-mantle boundary (CMB). We use the temperature profile from *Roberts and Arkani-Hamed* [2012] with the CMB temperature of T_{CMB} = 2000 K as the preimpact temperature profile (see Figure 1). The temperature increases adiabatically in the core as

$$\frac{dT}{dr} = -\frac{\alpha_{Fe} g(r) T}{c_{p,Fe}} \tag{6}$$

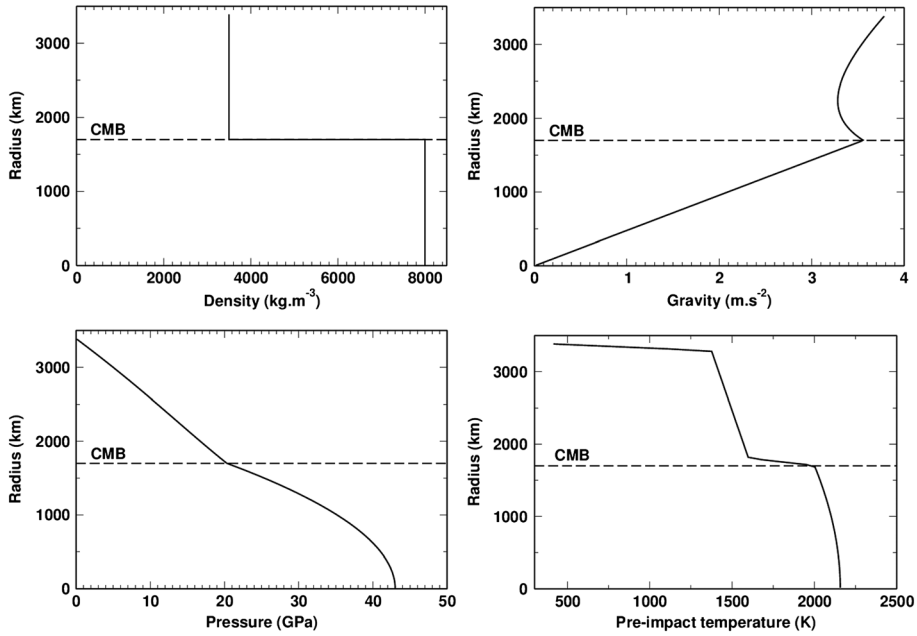

Figure 1. The preimpact density, gravity, pressure, and temperature profiles of the Mars model.

With the linear increase of gravity in the core (equation 2) and assuming constant thermal expansion coefficient α_{Fe} and heat capacity $c_{p,Fe}$, the integration of equation 6 leads to [e.g., *Coradini et al.*, 1983]

$$T_{\text{core}}(r) = T_{\text{CMB}} \exp\left(\left(\frac{2\pi\alpha_{\text{Fe}} G\rho_{\text{Fe}}}{3c_{p,\text{Fe}}}\right)\left(R_{\text{core}}^2 - r^2\right)\right) \tag{7}$$

Included in Figure 1 is the preimpact temperature profile used in our models.

3. Postimpact Temperature and Chemical Repartition

After a giant impact, the shock wave propagation results in a large thermal anomaly in the upper mantle of the planet [e.g., *Tonks and Melosh*, 1993; *Senshu et al.*, 2002; *Monteux et al.*, 2007; *Watters et al.*, 2009; *Arkani-Hamed and Olson*, 2010a, 2010b; *Roberts and Arkani-Hamed*, 2012]. Depending on the impact velocity and the efficiency of conversion from the kinetic energy to heat, the subsequent temperature increase may exceed the melting temperature of the mantle material [*Pierazzo et al.*, 1997; *Ghods and Arkani-Hamed*, 2011; *Monteux et al.*, 2011]. In the following section we describe our model of large impact heating of the Martian mantle and core.

3.1. The Impact-Induced Temperature Increase

Following a giant impact, a nearly uniform shock pressure P_s is generated inside the so-called isobaric sphere of radius r_c, [*Croft*, 1982; *Melosh*, 1989]

$$P_s = \rho_{\text{Si}}(C_0 + S\,u_o)\,u_o \tag{8}$$

where ρ_{Si} and C_0 are the preshock density and acoustic velocity of the silicate mantle, u_o is the particle velocity in the isobaric sphere, which is taken to be one half the impact velocity v_{imp} assuming similar target and impacting materials, and S is a constant. D_{imp} is the impactor diameter and v_{imp} is in km/s [*Arkani-Hamed and Olson*, 2010a, 2010b] of $r_c = 0.0525\, D_{\text{imp}}\, v_{\text{imp}}$. The shock pressure decays with distance from the impact site outside the isobaric region. Several different models have been proposed for the shock pressure distribution outside the isobaric region [*Ahrens and O'Keefe*, 1987; *Melosh*, 1989; *Pierazzo et al.*, 1997; *Mitani*, 2003]. In this study, we adopt the average model of *Pierazzo et al.* [1997]. Accordingly, the shock pressure P_s at a distance d from the isobaric center is calculated by

$$P_s(d) = P_s(r_c)\cdot(r_c/d)^n \qquad d > r_c; n = -1.84 + 2.61\log v_{\text{imp}} \tag{9}$$

The axisymmetric shock pressure in the Martian interior is calculated at 1×1 km grid intervals in a spherical coordinate system with the symmetry axis passing through the impact site and the planet's center. The

Table 1. C_0 and S Values for the Dunite

C_0 (m/s)	S	Reference
6600	0.86	*McQueen et al.* [1967], $P < 44$ GPa
5600	1.2	*McQueen et al.* [1967], $P > 45$ GPa
5500	1.80	*Ahrens and Johnson* [1995]
5140	1.12	*Trunin* [2001], $29.8 < P < 102.1$ GPa
5120	1.27	*Trunin* [2001], $30.6 < P < 223.7$ GPa
7800	0.2	*Melosh* [1989], $44 < P < 73$ GPa
4400	1.5	*Melosh* [1989], $P > 73$ GPa

pressure reduction near the surface due to interference of the direct and reflected waves is taken into consideration after modifying *Melosh*'s [1989] rectangular coordinate algorithm to a spherical coordinate algorithm [*Shahnas and Arkani-Hamed*, 2007; *Louzada and Stewart*, 2009]. At the core-mantle boundary the incident pressure wave is partly reflected to the mantle and partly transmitted to the core [*Arkani-Hamed and Ghods*, 2011]. The interference of the direct and reflected waves in the mantle near the core-mantle boundary has only minor effects on the shock pressure and is neglected.

As the impact-induced shock wave propagates in the planet it creates a high pressure behind the shock front and sets the material in motion. The pressure behind the shock front is determined using the conservation of momentum across the front,

$$P_s - P_o = \rho_o u\, U. \tag{10}$$

where u and U are the particle and shock wave velocities, respectively. P is the total pressure (shock pressure plus the preshock lithostatic pressure) behind the shock front. P_o and ρ_o are the preshock lithostatic pressure and density ahead of the shock front, which are radially dependent (Figure 1). We also use an empirical, linear Equation of State (EOS) to relate the shock wave velocity to the particle velocity,

$$U = C_0 + S\, u. \tag{11}$$

The acoustic velocity C_0 (= $(K/\rho_o)^{1/2}$, K is the bulk modulus) and the parameter S are pressure and temperature dependent in general. We assume they are constant in our models, with different values in the core and the mantle. Table 1 is a list of measurements for dunite, which is probably a reasonable candidate for the mantle material. The S values of 1.8 by *Ahrens and Johnson* [1995] and 0.2 by *Melosh* [1989] are well off compared to the others. In our models C_0 ranges between 5140 and 6965 m/s and S between 0.8 and 1.12. The $C_0 = 6965$ (m/s) is the average value in the upper mantle of the Earth, from the base of the crust down to 670 km transition zone which is comparable to Martian interior as far as temperature and pressure is concerned, determined using the PREM model of the Earth [*Dziewonski and Anderson*, 1981].

The shock-induced temperature increase ΔT is determined following the "foundering" model of *Watters et al.* [2009] (see Figure 2, bottom left),

$$\Delta T = \left\{ P_\delta (1 - 1/f)/(2\,\rho_o S) - (C_0/S)^2 (f - ptln\, f - 1) \right\}/C_p, \tag{12}$$

where

$$f = -P_\delta / \left(\beta \left\{ 1 - \left[(2\,P_\delta/\beta) + 1^{1/2} \right] \right\} \right), \tag{13}$$

$$P_{\delta =} P_s - P_o, \tag{14}$$

$$\beta = \left({C_0}^2 \rho_o \right)/(2\,S), \tag{15}$$

P_o is the preshock lithostatic pressure, ρ_o stands for the preshock density, and C_p is the specific heat of the mantle.

3.2. Postimpact Melting and Thermal Mixing

The temperature field below the impact site and before the core merging is obtained by adding the preimpact temperature profile $T_0(r)$ and the impact-induced temperature increase $\Delta T(r,\theta)$. Considering that the preimpact mantle is solid, the postimpact temperature can exceed the solidus temperature of silicates within the Martian mantle, consume latent heat, and generate a large partially to completely molten zone. The latent heat of melting is accounted for in the heat budget. For simplicity, we consider that the solidus (T_{sol}) and the liquidus (T_{liq}) temperatures of silicates are constant with depth and $T_{sol} = 1800$ K and $T_{liq} = 2300$ K [*Ghods and Arkani-Hamed*, 2007]. Truly, T_{sol} and T_{liq} are also pressure dependent [*Katz et al.*, 2003; *Roberts and Barnouin*, 2012]. The iron core of the impactor is assumed to be molten prior to the impact and no latent heat is consumed to melt it.

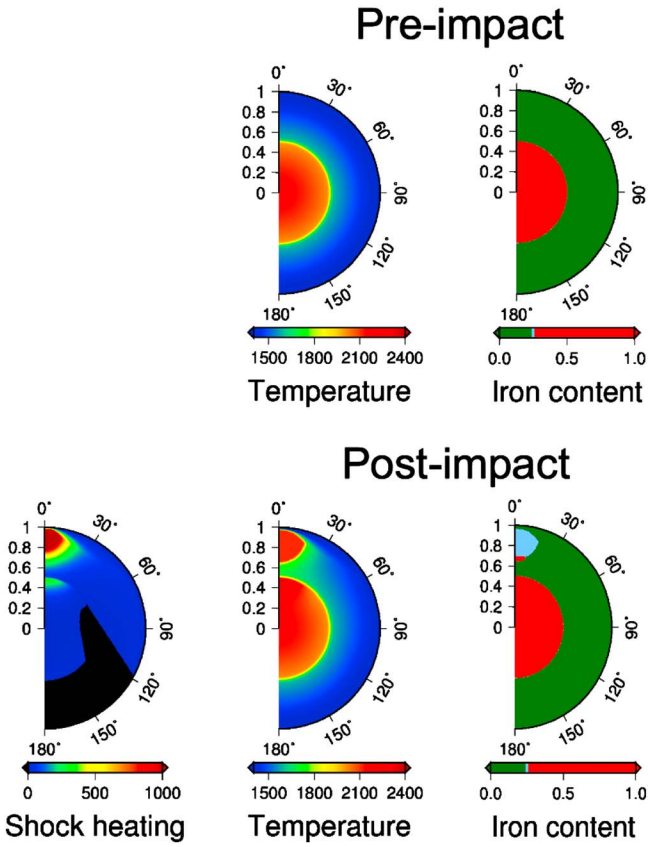

Figure 2. Preimpact temperature (in K)/compositional fields, shock-induced temperature increase (in K), and postimpact temperature (in K)/compositional fields after a 750 km diameter impact with $C_0 = 6000$ m/s and $S = 0.86$ (Reference case). In the right bottom figure, the blue colored material represents partially molten silicates.

For a given mantle volume, the potential temperature $T(r, \theta) = T_0(r) + \Delta T(r, \theta)$ must be modified to take into account the latent heat of melting. The fraction of melt f_{melt} is calculated as follows. For a potential temperature larger than $(T_{liq} + L_{Si}/C_{pSi})$ melting is complete ($f_{melt} = 1$) and the latent heat consumption leads to a temperature reduction from T to T' following

$$T'(r,\theta) = T(r,\theta) - L_{Si}/C_{pSi}. \quad (16)$$

For a potential temperature lower than the T_{sol}, $f_{melt} = 0$ and no latent heat is consumed

$$T'(r,\theta) = T(r,\theta). \quad (17)$$

Where the potential temperature T ranges between T_{sol} and $T_{liq} + L_{Si}/C_{pSi}$, the latent heat consumption linearly increases within the partially molten region and

$$T'(r,\theta) = \left[C_p T(r,\theta)\left(T_{liq} - T_{sol}\right) + T_{sol} L_{Si}\right] / \left[C_{pSi}\left(T_{liq} - T_{sol}\right) + L_{Si}\right] \quad (18)$$

After the impact heating and melting, mechanical mixing due to segregation of iron occurs within the partially molten region leading to a homogenization of the temperature where partial melting occurs [*Senshu et al.*, 2002; *Deguen et al.*, 2011]. The efficiency of mixing increases with the size of the planet and gravitational energy released per impactor mass [*Pierazzo et al.*, 1997; *Deguen et al.*, 2011]. Hence, in the partially to completely molten volume, called hereafter the segregation volume, both silicates and iron are in thermal equilibrium. As a rough estimate we determine the temperature inside the segregation volume by volume averaging the temperatures of the partially and completely molten material.

The final postimpact temperature field strongly depends on D_{imp}, C_0 and S (see Table 2). Figure 2 (second column) shows the preimpact and postimpact temperature fields for $D_{imp} = 750$ km, $C_0 = 6000$ m/s, and $S = 0.86$ model,

Table 2. Free Parameters Range Studied in Our Models

Parameter	Description	Value
C_0	Acoustic velocity of the mantle	5140, 6000, and 6965 m/s
	Acoustic velocity of the core	3800 m/s
S	EOS Constant of the mantle	0.8, 0.86, and 1.12
	EOS Constant of the core	1.6
v_{imp}	Impact velocity	10 km/s
D_{imp} (=2 R_{imp})	Impactor diameter	500, 750, and 1000 km
η_0	Reference viscosity	10^{20}–10^{22} Pa s
ρ_0	Mean density	4060 kg m^{-3}
ρ_{Si}	Mantle density	3500 kg m^{-3}
ρ_{Fe}	Core density	7500 kg m^{-3}
c_T	Temperature-induced viscosity contrast	10–1000
c_Z	Pressure-induced viscosity contrast	10
c_1	Temperature-induced viscosity contrast (if $f_{melt} = 0$)	10–1000
c_2	Melt-induced viscosity contrast (if $f_{melt} > 0$)	30–3000

which is designated as our reference model for the rest of the study. The impact angle should also influence the shape of the postimpact thermal anomaly and, hence, the shape of the segregation volume where melting occurs [*Pierazzo and Melosh*, 2000]. Indeed, increasing the impact angle from 0° (head-on impact) to larger values (oblique impacts) reduces the volume of the impact melt. Here we consider the upper limit case of a vertical impact where the efficiency of melt production is optimal.

3.3. Postimpact Chemical Repartition

Assuming that the bulk chemistry of the impactor is the same as Martian (12.5% volume of the metallic phase), a metallic volume with an equivalent radius $R_{Fe} = R_{imp}/2$ is retained when the planet is hit by an impactor with a radius R_{imp}. The retained impactor's core is denser than the silicates and rapidly sinks and fills the bottom of the segregation volume [*Monteux et al.*, 2009; *Deguen et al.*, 2011]. This leads to the formation of a complex shape diapir that starts to sink toward the Martian core while deforming the relatively colder and more viscous surrounding mantle (see Figure 2, third column).

4. Dynamic Model of Core Merging

Once buried below the surface, the dense metallic core of the impactor sinks toward the center of the target planet. Dissipation of the work done by buoyancy forces driving motion of this diapir occurs and causes heating in the mantle and/or the diapir.

4.1. Physical Model

To investigate the dynamics of the metallic diapir, we follow the procedure adopted by *Monteux et al.* [2009] and assume that the mantle deforms in a diffusion creep limit. Briefly, the conservation of energy leads to

$$\frac{DT}{Dt} = \frac{\nabla^2 T}{Ra_\chi} + Di\left(\frac{\eta}{\eta_0} B\Omega - v_r\left(T + \frac{T_0(r)}{\Delta T_0}\right)r\right) \quad \text{with} \quad \frac{D}{Dt} = \frac{\partial}{\partial t} + (v\cdot\nabla) \tag{19}$$

T, t, r, and v_r are dimensionless temperature, time, radius, and radial velocity, respectively. $Ra_\chi = \frac{\Delta\rho_0\, g_0\, R^3}{\kappa\eta_0}$ is the compositional Rayleigh number and $Di = \frac{\alpha\rho_0 g_0 R}{\overline{\rho_0 C_p}}$ is the dissipation number (with κ the heat diffusivity and $\overline{\rho_0 C_p}$ the average volume specific heat of the impacted body). $B = \frac{\Delta\rho_0}{\rho_0 \alpha \Delta T_0}$ is the chemical/thermal buoyancy ratio, where ρ_0 and α are the average density and thermal expansion of the planet. The density difference, which drives the flow, is a function of temperature and chemical composition. Because $B >> 1$, the influence of the chemical difference between iron and silicates is preponderant in the density difference. The temperature-, pressure-, and melt-dependent viscosity is η, and η_o is a constant reference viscosity. The dimensionless dissipation function Ω expresses the conversion of potential energy into heat through viscous dissipation,

$$\Omega = 2\underline{\varepsilon} : \underline{\varepsilon} \tag{20}$$

where $\underline{\varepsilon}$ is the dimensionless shear strain rate tensor. The preimpact temperature $T_0(r)$ is radially dependent.

Assuming an incompressible medium with an infinite Prandtl number, the conservation of mass and momentum are expressed as

$$\nabla\cdot v = 0 \tag{21}$$

and

$$-\nabla P + \nabla\cdot\left(\frac{\eta}{\eta_0}\left[\nabla v + [\nabla v]\right)\right) + \left(\frac{T}{B} - f\right) re_r = 0 \tag{22}$$

where v and P are the nondimensional velocity and pressure and e_r is the radial unit vector. The buoyancy force that drives the diapir toward the center of the planet increases with the volume fraction of metal f that varies between 1 (pure metal) and 0 (pure silicates). The f is simply advected by the flow

$$\frac{Df}{Dt} = 0. \tag{23}$$

4.2. Viscosity Model

After ponding at the bottom of the segregation zone, the dense metallic phase sinks toward the core of the impacted planet. How this occurs is debated. Proposed mechanisms include percolation through a solid mantle [*Shannon and Agee*, 1996; *Stevenson*, 1990], settling of centimeter-sized droplets in a magma ocean

[*Rubie et al*., 2003] and large mantle diapirs [*Ricard et al*., 2009; *Senshu et al*., 2002; *Tonks and Melosh*, 1992]. In addition, it has been proposed that metallic diapirs can sink toward the centers of the planets via fracturing and diking [*Tonks and Melosh*, 1992; *Solomatov*, 2000; *Stevenson*, 2003] or via viscous deformation [*Honda et al*., 1993; *Monteux et al*., 2009] depending on the thermal state of the planets' mantle. In the frame of the impactor's core sinking as a single large metallic diapir, the rheology of the Martian mantle plays a key role since it governs its ability to deform during the merging. Under the conditions of a massive iron diapir sinking through solid mantle the large deviatoric stress generated by the diapir could lead to a nonlinear rheology [*Samuel and Tackley*, 2008; *Golabek et al*., 2009], elastoplastic deformations [*Gerya and Yuen*, 2007] or even to fracturing if they exceed the ultimate strength of rocks which is ~1–2 GPa [*Davies*, 1982].

However, several lines of evidence suggest the viscous deformation considered in the present study to be a more likely mechanism: (1) Detailed study of the distance from Mars to Phobos, the motion of the shadow of Phobos on the surface of Mars measured by Mars Orbiter Laser Altimeter, and the Viking I Lander observation of the motion of the shadow of Phobos passing over it led *Bills et al*. [2005] to suggest that the mantle of Mars at present is more deformable than that of the Earth, (2) in its early history, because of the combination of the heating from accretion and short-lived radioisotopes, and from conversion of potential energy during core formation, the Martian mantle was probably much hotter and softer than today [*Senshu et al*., 2002; *Breuer et al*., 2010], and more importantly (3) the iron diapir sinks through the already impact-heated region of the mantle below the segregation zone. Included in Figure 2 (second row, middle) is the temperature field immediately after a 750 km diameter impact (other temperature fields obtained from the different impact parameters investigated in this study will be represented later in Figures 5, 7, and 8). The temperature directly beneath the segregation zone is much closer to the solidus of the mantle, implying that the metallic core likely sinks via diffusional flow deformation (Newtonian flow) [*Honda et al*., 1993; *Monteux et al*., 2013]. Hence, excluding power law rheologies and plasticity seems to be reasonable as a first-order approximation. However, as the mantle viscosity in early Mars may be sufficiently large to support large stresses, more sophisticated models considering these two effects might be envisioned. Due to the numerical limitations of our model, this is currently beyond the scope of the present study.

To account for the viscosity contrast between the hot molten material and the cold solid material, we adopt a temperature-, melt-, and pressure-dependent viscosity model:

$$\eta\,(T,P)/\eta_0(T_0,P_0) = \exp(-c_T T + c_Z P). \tag{24}$$

where $\eta_0 = \eta(T_0,P_0)$ is the viscosity of the cold and shallow undifferentiated material at the start of the experiment, c_Z is a constant, and c_T depends on the melt fraction of the material. For completely solid, c_T equals c_1, and c_2 for completely molten regions (see Table 2). In the partially molten region c_T is linearly interpolated between c_2 and c_1,

$$c_T = (c_2 - c_1)/\left(T_{\mathrm{liq}} - T_{\mathrm{sol}}\right)T(r,\theta) + c_1 - (c_2 - c_1)/\left(T_{\mathrm{liq}} - T_{\mathrm{sol}}\right)\, T_{\mathrm{sol}}. \tag{25}$$

This type of viscosity model decreases sharply with temperature and its expression is simpler to implement than the usual Arrhenius law [*Ratcliff et al*., 1997; *Ziethe and Spohn*, 2007]. We neglect the compositional dependency of the viscosity for two reasons. First, the compositional contrasts are sharp and may lead to steep viscosity fronts, difficult to handle numerically. Second, among the parameters that might affect the viscosity (composition, temperature, melting degree, and pressure) experimental results suggest that the viscosity contrast is more sensitive to the melting degree and temperature. Ultimately, the viscosity contrast between hot molten iron (or fully molten silicates) and solid cold silicates can reach 20 orders of magnitude [*Vocadlo et al*., 2000].

To model the influence of the viscosity contrast between hot molten iron and cold solid silicates on the core merging dynamics, we use much smaller contrast. This approach is encouraged by the fact that the viscosity of the surrounding silicate material mainly governs the merging velocity [*Hadamard*, 1911; *Batchelor*, 1967]. Diapirs more than 10 times less viscous than the wall rock will behave like inviscid diapirs [*Weinberg and Podladchikov*, 1994]. However, shear-heating partitioning is strongly dependent on the viscosity contrast between the two media [*Ke and Solomatov*, 2009; *Monteux et al*., 2009]. In our study we consider two end-member viscosity models: models where the viscosity remains uniform and constant and models where the hot diapir is initially 10^3 times less viscous than the coldest mantle. Further viscous heating during the core merging can eventually increase the viscosity contrasts up to 10^4. Incorporating larger viscosity contrasts leads to numerical instabilities.

4.3. Numerical Model

The above dynamic equations are solved in an axisymmetric spherical geometry using 200×400 to 400×800 grid points in the r and θ directions. An implicit inversion method [*Schubert et al*., 2001] is adopted for the momentum equation and an Alternating Direction Implicit scheme [*Peaceman and Rachford*, 1955; *Douglas*, 1955] for the energy and mass conservation. The numerical diffusion in solving the transport equations, especially for the compositional field, is constrained using total variation diminishing Superbee scheme [*Roe*, 1986; *Laney*, 1998] in an implicit procedure [*Šrámek et al*., 2010], which enables a high resolution of pure advective fields. Free-slip velocity is imposed at the surface and along the axis of symmetry. The core-mantle boundary is a mobile interface that can deform in response to the merging of the impactor's core. Thermal boundary conditions are isothermal at the surface and insulating along the symmetry axis. The spherically symmetric boundary conditions are applied at the center of the planet.

4.4. Simplifications

A number of approximations are made in the numerical models to simplify the analysis of the core merging process:

1. We assume that the heat capacities per unit volume of iron and silicates are equal and representative of a mixture: $\overline{\rho C_p} = \rho_{\mathrm{Fe}} C_{p,\mathrm{Fe}} = \rho_{\mathrm{Si}} C_{p,\mathrm{Si}}$. Actually, $\rho_{\mathrm{Fe}} C_{p,\mathrm{Fe}} = 4500$ kJ K^{-1} m^{-3} and $\rho_{\mathrm{Si}} C_{p,\mathrm{Si}} = 4200$ kJ K^{-1} m^{-3}. We use $\overline{\rho C_p} = 4312$ kJ K^{-1} m^{-3}.
2. The characteristic diffusion time ($\propto R_{\mathrm{Fe}}^2/\kappa$) during the core merging is much larger than the characteristic sinking time $\left(\propto \frac{\eta_0}{\Delta\rho_0 g R_{\mathrm{Fe}}}\right)$ even with the metallic thermal conductivity k_{Fe} (= 40 W m^{-1} K^{-1}) [*Stacey and Anderson*, 2001] larger than the silicate thermal conductivity k_{Si} (= 3–4 W m^{-1} K^{-1}) [*Hofmeister*, 1999]. Hence, the heat diffusion during the sinking is negligible and the thermal conductivities for metallic and silicate material are assumed to be equal.
3. The heat partitioning during the metal/silicate separation is strongly dependent on the mechanisms of iron segregation. If liquid iron is transported to the center of the planet through channels, the potential energy related to core formation would largely go into the core [*Ke and Solomatov*, 2009]. However, when the liquid metal is transported via a large diapir and depending on the viscosity contrast between the diapir and the surrounding silicates, the potential energy of the diapir that is released via viscous heating heats the surrounding silicates causing further melting [*Ke and Solomatov*, 2009; *Monteux et al*., 2009; *Samuel et al*., 2010]. Also, crystallization of the molten silicate occurs especially near the cold Martian surface. These two processes can influence the heat budget and affect the temperature evolution. Moreover, the viscous heating can have consequences on the rheology of the material surrounding the diapir and modify the sinking dynamics. In our dynamic model of core merging, we do not consider any *consumption* or release of latent heat during the sinking of the diapir. However, in the melt-dependent viscosity models, the viscosity increases abruptly by a factor of c_2 when temperature within a grid cell decreases below the solidus. On the opposite, when the temperature within a grid cell exceeds T_{liq} its viscosity is reduced abruptly by a factor c_2 (see Table 2 for values).
4. During the sinking of the large volume of the impactor's iron core, the gravity field locally and temporally changes slightly. We neglect the changes of the gravity during the sinking.
5. The impactor's iron core, the silicate mantle, and the iron core of the planet are considered in the infinite Prandtl number regime. In reality, the molten metallic cores have viscosities that are about 20 orders of magnitude smaller than the mantle viscosity. Such large but realistic viscosity contrasts may have consequences on both the sinking and the merging dynamics and may affect the heat dissipation during the sinking [*Ke and Solomatov*, 2009; *Monteux et al*., 2009, 2011; *Samuel et al*., 2010]. However, in the case of Newtonian rheology as considered here, increasing the viscosity contrast between the hot liquid diapir and the surrounding silicates may not significantly change the sinking velocity of the diapir which is mainly controlled by the mantle viscosity [*Hadamard*, 1911; *Rybczynski*, 1911; *Yiantsios and Davis*, 1990]. Diapirs more than 10 times less viscous than the wall rock will behave like inviscid bubbles and further decrease in viscosity will not alter the behavior [*Hadamard*, 1911; *Rybczynski*, 1911; *Weinberg and Podladchikov*, 1994]. When considering a power law rheology, a large viscosity contrast between the diapir and the mantle might affect the terminal velocity of the diapir and induce differences with the theoretical velocities predicted with a Newtonian rheology [*Weinberg and Podladchikov*, 1994].

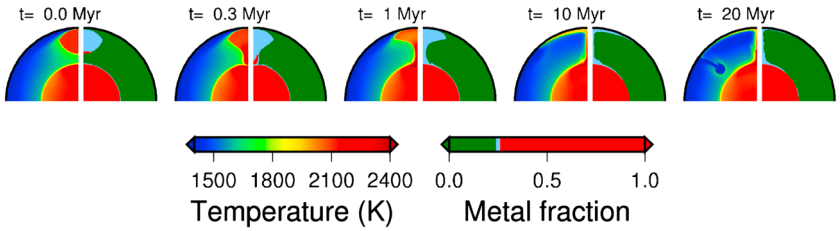

Figure 3. (left to right) Thermochemical readjustment for the model with $D_{imp} = 750$ km, $C_0 = 6000$ m s^{-1}, $S = 0.86$, and $\eta_0 = 10^{21}$ Pa s (isoviscous) at certain times after the impact. In each panel the left part shows the temperature distribution, and the right part shows the iron fraction. The blue colored material in the right part represents partially molten silicates.

5. Reference Model (Influence of the Initial Shape)

Figure 3 shows the thermochemical evolution for the reference model where $D_{imp} = 750$ km, $C_0 = 6000$ m s^{-1}, $S = 0.86$, and $\eta = 10^{21}$ Pa s (isoviscous). The dense iron diapir rapidly sinks toward the planet's core. During the sinking, the potential energy of the diapir is converted into heat via viscous dissipation and heats both the mantle and the diapir. The diapir becomes slightly hotter than the Martian core and spreads on the core in a short time. However, because of the small density difference between the molten and solid silicates, it takes much longer time for the hot and molten silicates to ascend and spread beneath the rigid lithosphere of the planet, potentially forming a magma ocean. The spreading is followed by the initiation of convection in the Martian mantle where a cold slab sinks toward the CMB from the edge of the hot magma ocean.

During sinking, the metallic diapir deforms the surrounding mantle over a radial distance that depends on the diameter of the diapir, the effective viscosities of the mantle and the diapir, the distance between the diapir and the planet's core (i.e., the gap thickness), and the density difference across the CMB. The core of the planet has a minor effect on the dynamics of the diapir at a large gap thickness and the diapir sinks with a Stokes-like velocity [*Batchelor*, 1967; *Monteux et al*., 2013]. When the gap thickness is small, the mantle flow that enables the diapir sinking is confined between two mechanical boundary layers, one at the bottom of the diapir and the other at the top of the core. The horizontal shear stress in these boundary layers hampers the sinking of the diapir, and the sinking velocity decreases.

In Figure 4 (top, black lines), we monitor the gap thickness for our reference case. The gap thickness is calculated using the composition profile along the symmetry axis and particularly the difference in positions where the second derivative is zero. Because of some numerical diffusion of the compositional field, the final gap thickness of our models is slightly larger than the vertical spatial resolution of our models. As illustrated also in Figure 4 (top, black lines), the final gap thickness decreases for higher numerical resolutions. We consider that the time when the final gap thickness is reached corresponds to the "merging time" $t = t_m$ (i.e., the two cores are about to enter physically in contact). The characteristic coalescence time t_c in case of a spherical diapir is [*Monteux et al*., 2013]

$$t_c = \frac{2\lambda_0 \eta_0}{a_1 \Delta\rho_0 g_0 R_{Fe}} \left(\frac{h_0}{R_{Fe}}\right)^{1/2} \tag{26}$$

where λ_0 is the mantle viscosity/diapir viscosity ratio, h_0 is the initial gap thickness, and a_1 is a geometrical constant that is typically on the order of 0.1 for the isoviscous case and 0.2 for the T-dependent viscosity [*Monteux et al*., 2013]. Calculating the characteristic coalescence time from equation 26, we obtain a characteristic sinking time $t_c = 0.36$ Myr. From Figure 4 (top, black lines), we observe that our numerical results (where the merging time ≈ 0.36–0.47 Myr) are in agreement with the theoretical coalescence time of the spherical diapir and that the initial shape of the diapir does not significantly affect the sinking time [*Weinberg and Podladchikov*, 1994]. An elongated diapir could increase the surface contact between the iron and the silicated material, potentially increasing the chemical degree of equilibration. However, the sinking time is too short for such a chemical equilibration.

6. Influence of C_0, S, and D_{imp}

This section characterizes the influence of C_0, S, D_{imp} for different viscosity models. The characteristics of these models and the main results are listed in Table 3. In particular we monitor the merging temperature T_m which is

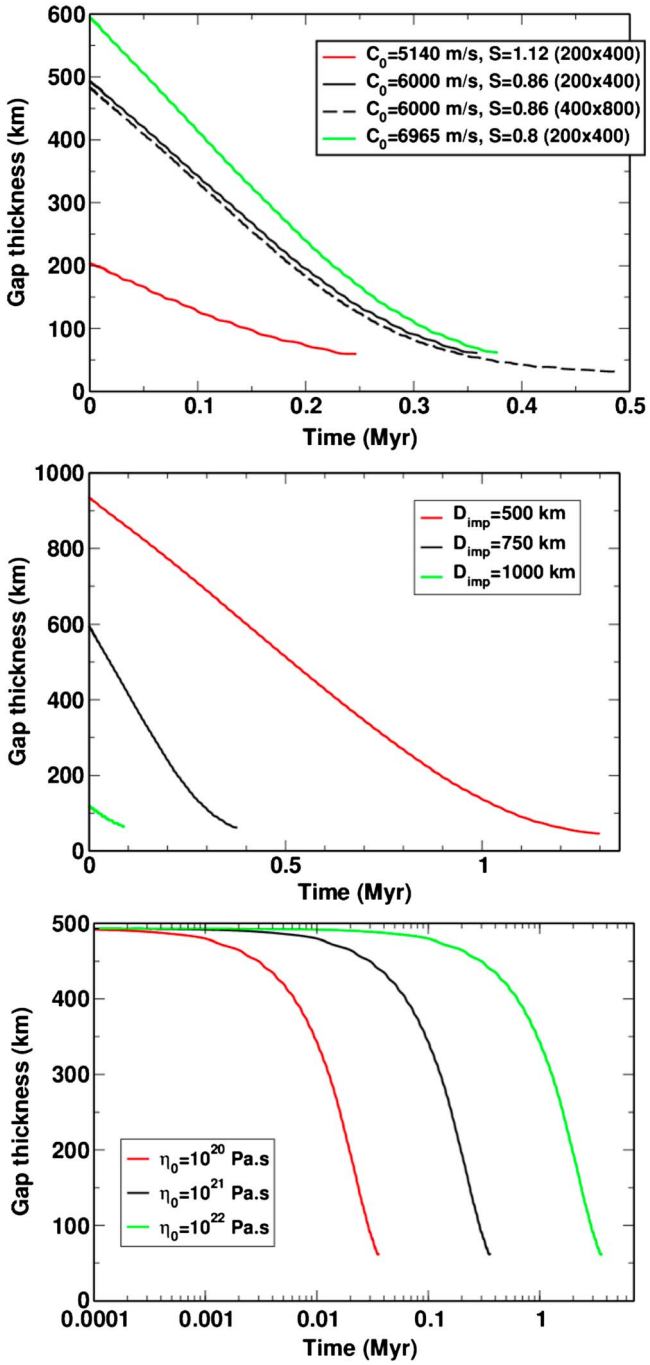

Figure 4. Gap thickness evolution for models with different (C_0, S) sets of (top) parameters, (middle) impactor diameters D_{imp}, and (bottom) reference viscosities η_0.

the average temperature within the sinking diapir when $t = t_m$. The initial gap thickness is a function of the postimpact segregation volume. Hence, it depends on the (C_0, S) set of parameters and on the impactor size. We monitor the thermochemical evolution after a large impact on Mars using different sets of parameters C_0, S, and D_{imp}.

Figure 5 (first column) illustrates the influence of C_0 and S on the postimpact segregation volume and hence on the thermochemical state before the merging process. For the three sets of (C_0, S) examined, the initial temperature within the segregation volume slightly varies and is $\approx 2100 \pm 10$ K. When C_0 increases and S decreases a smaller segregation volume is generated after the impact. On the other hand, when C_0 decreases and S increases, the size of the segregation volume increases. Hence, the impactor's core is initially closer to the CMB (Figure 5, top). Consequence, the core merging occurs in a short time (Figure 4, top). Within the range of C_0, S studied here the sinking time (i.e., the time needed for the two cores to enter in contact) can decrease by $\approx 35\%$ (from 0.38 Myr for ($C_0 = 6965$ m s^{-1}, $S = 0.8$) to 0.25 Myr for ($C_0 = 5140$ m s^{-1}, $S = 1.12$)) (Figure 6, right). As C_0 and S control the shape of the segregation volume and especially the initial gap thickness between the two cores, these parameters play also a significant role on the temperature of the diapir immediately before merging. Within the range of C_0, S studied here the merging temperature can increase by $\approx 10\%$ (from 2130 K for ($C_0 = 5140$ m s^{-1}, $S = 1.12$) to 2350 K for ($C_0 = 6965$ m s^{-1}, $S = 0.8$)) which can have important consequences on the preexisting core cooling after merging (Figure 6, left).

The Martian topographic dichotomy is related to an impact ranging from 800 to 1300 km in diameter [*Marinova et al.*, 2008; *Andrews-Hanna et al.*, 2008; *Nimmo et al.*, 2008]. In our models, we consider that the impactor's core is collected at the bottom of the segregation volume. When the impactor is too large ($D_{imp} > 1000$ km), the segregation volume is in contact with the Martian core, and the merging dynamics is governed by the viscosities of the molten silicates and the liquid iron. Hence, the merging dynamics involves turbulent flows and our models are no more valid. Therefore, we limit our study to impactor diameters ranging from 500 km to 1000 km. Moreover, as detailed above, decreasing C_0 and increasing S would increase the size of the segregation volume, and for $D_{imp} = 1000$ km, $C_0 < 6965$ m s^{-1} and $S > 0.8$, the

Table 3. Model Specifics

Model	Impactor Diameter (Shell Thickness) (km)	C_0 (m/s)	S	Reference Viscosity (Pa s)	Viscosity Contrast	Merging Time (Myr)	Merging Temperature (K)
M0 (ref.)	750 (0.8)	6000	0.86	10^{21}	1	0.36	2286.7
M1	750 (0.8)	6965	0.8	10^{21}	1	0.37	2352.5
M2	750 (0.8)	5140	1.12	10^{21}	1	0.24	2137.6
M3	1000 (1.8)	6965	0.8	10^{21}	1	$8.9\ 10^{-2}$	2127.7
M4	500 (0.2)	6965	0.8	10^{21}	1	1.3	2392.9
M5	750 (0.8)	6000	0.86	10^{20}	1	$3.6\ 10^{-2}$	2287.3
M6	750 (0.8)	6000	0.86	10^{22}	1	3.6	2280.5
M7	750 (0.8)	6000	0.86	10^{21}	10 (*T-P*)	0.1	2281.6
M8	750 (0.8)	6000	0.86	10^{21}	10 (*T-P* melt)	$6.3\ 10^{-2}$	2290.1
M9	750 (0.8)	6000	0.86	10^{21}	100 (*T-P*)	$1.3\ 10^{-2}$	2277.4
M10	750 (0.8)	6000	0.86	10^{21}	100 (*T-P* melt)	$7.5\ 10^{-3}$	2323.2
M11	750 (0.8)	6000	0.86	10^{21}	1000 (*T-P*)	$1.5\ 10^{-3}$	2292.5
M12	750 (0.8)	6000	0.86	10^{21}	1000 (*T-P* melt)	$1.0\ 10^{-3}$	2301.3

segregation volume also overlaps the CMB. Hence, to measure the influence of the impactor size, we only consider $C_0 = 6965$ m s^{-1} and $S = 0.8$. Figure 7 shows the merging dynamics for three impactor diameters. When D_{imp} increases, the segregation volume and the metallic volume of the impactor increase. However, the mean temperature of the segregation volume is not significantly affected (differences of ≈ 10 K between $D_{imp} = 500$ km and $D_{imp} = 1000$ km) (Figure 6, left). The major difference resides in the volume of the postimpact segregation zone of the planet which is much more significant for $D_{imp} = 1000$ km (see Figure 7, third row). When the impactor diameter increases, the volume of the segregation zone and the size of the merging diapir increase, resulting in the reduction of h_0 and in the increase of R_{Fe}, which reduce the sinking time from ≈ 1 Myr for $D_{imp} = 500$ km to ≈ 0.1 Myr for $D_{imp} = 1000$ km (Figure 6, right). As D_{imp} controls the initial distance between the two cores, it also influences the temperature of the diapir before merging [*Monteux et al.*, 2009]. Hence, when D_{imp} increases from 500 to 1000 km, the impactor's core becomes initially closer to the CMB and h_0 decreases from 935 km to 120 km (Figure 4, middle). Hence, its available potential energy decreases, and the merging temperature decreases by ≈ 12 % (from 2400 to 2130 K) (see Figure 6, left).

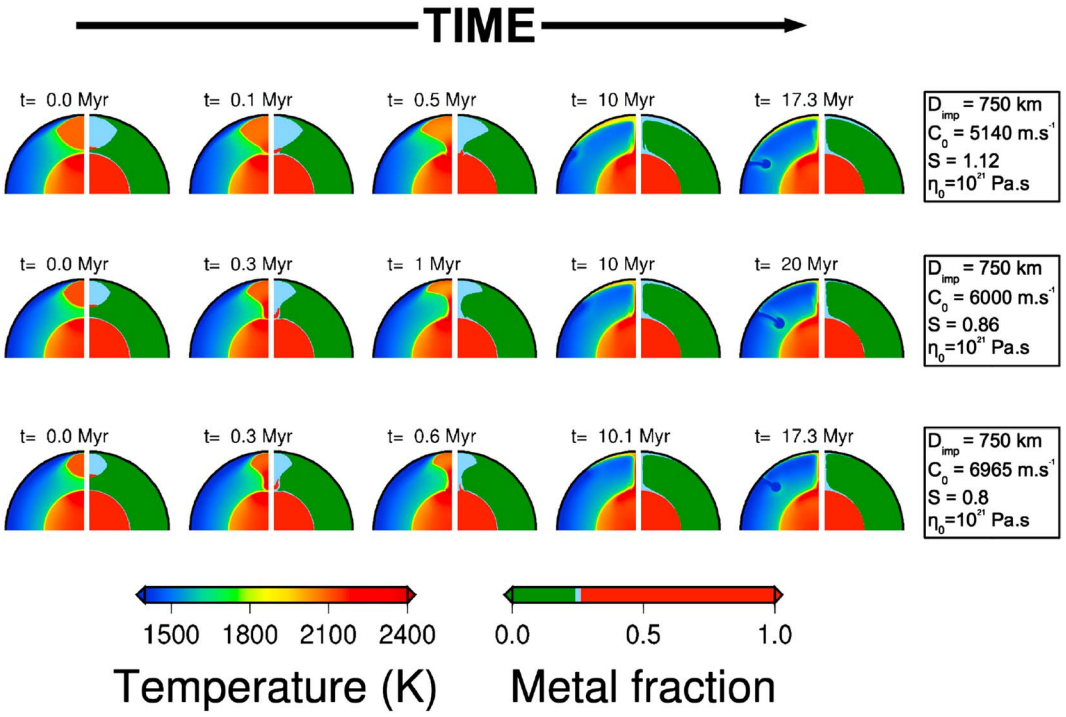

Figure 5. Thermochemical readjustment as a function of time for models with three (C_0, S) sets of parameters. We consider here that the viscosity η_0 is uniform and constant.

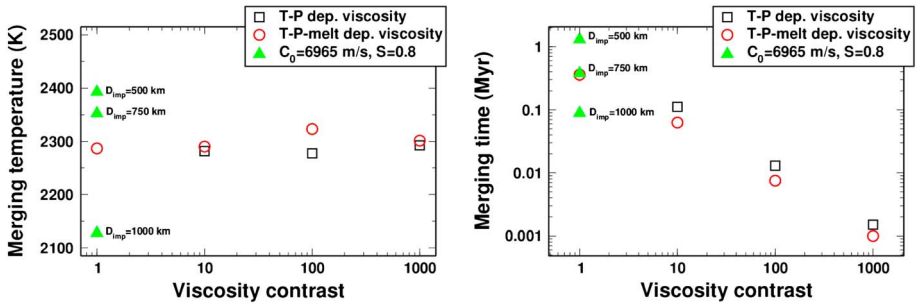

Figure 6. (left) Merging temperatures and (right) merging times as a function of the viscosity contrast. Green filled solid triangles represent results for uniform viscosities, with $C_0 = 6965$ m/s and $S = 0.8$ and for different impactor diameters (indicated close to the corresponding symbol). The open symbols represent the values obtained with $C_0 = 6000$ m/s and $S = 0.86$ for *T-P* dependent viscosities (black squares) and for *T-P* melt-dependent viscosities (red circles).

Finally, by controlling the segregation volume D_{imp}, C_0 and S indirectly control the final radial extension of the magma ocean spreading, and the position of the cold slab that sinks from the surface toward the CMB (see Figures 5 and 7).

7. Influence of the Viscosity Model

7.1. Influence of the Average Viscosity

The mantle viscosity is a key parameter in the core merging process that governs the ability of the mantle to deform and accommodate the metallic diapir sinking, while deforming at farther distances to compensate for the accommodation. The viscosity also governs the spreading of the hot silicate material in the upper mantle. When consider dynamical models with uniform viscosities (i.e., η_0 is constant and $c_T = c_Z = 0$), modifying the mean viscosity does change the heat repartitioning at the end of the merging and affects the characteristic

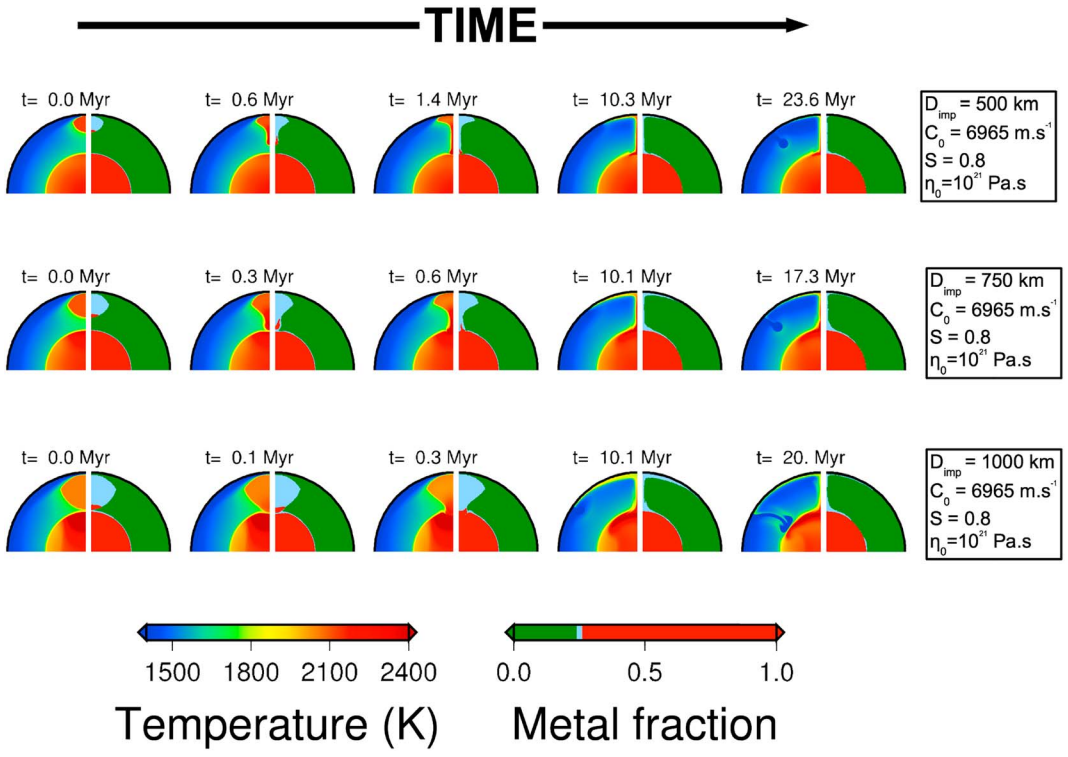

Figure 7. Thermochemical readjustment as a function of time for models with three impactor sizes. We consider here that the viscosity η_0 is uniform and constant. $C_0 = 6965$ m s^{-1} and $S = 0.8$.

merging and spreading times. In the laminar flow regime, the terminal sinking velocity U of a metallic diapir sinking in an infinite media obeys the Hadamard velocity law [*Hadamard*, 1911; *Batchelor*, 1967; *Monteux et al*., 2009]. As a consequence

$$U = \frac{2}{9}\left(\frac{\eta_d + \eta_s}{\eta_d + \frac{2}{3}\eta_s}\right)\frac{\Delta\rho_0 g {R_{\mathrm{Fe}}}^2}{\eta_s} \tag{27}$$

where η_d is the viscosity inside the diapir and η_s is the viscosity of the surrounding material. In the isoviscous case (Figure 4, bottom) when the average viscosity of the mantle decreases the diapir sinks faster (see equation 27), and the sinking time is significantly reduced. For example, in an isoviscous model, $\eta_d = \eta_s$, increasing the viscosity from 10^{20} Pa s (Figure 4, bottom, red line) to 10^{22} Pa s (Figure 4, bottom, green line) leads to an increase of the sinking times from ≈ 0.1 Myr to ≈ 10 Myr (Table 3). Similarly, an increase of the average viscosity by 2 orders of magnitude increases the spreading time of the hot mantle thermal anomaly from ≈ 1 Myr to ≈ 100 Myr, even if the thermal anomaly cools by diffusion. However, the changes in the average uniform viscosity have less effects on the merging temperatures that range between 2280 and 2290 K at $t = t_m$ (Table 3). For large viscosities, as the characteristic merging and spreading times are longer, heat diffusion plays a significant role and smoothes the temperature contrasts between the hot merging channel and the surrounding silicates, at the CMB, and between the sinking slab and the colder surrounding mantle.

7.2. Influence of Varying Viscosity

The viscosity contrast between the sinking diapir and its surroundings is a key parameter in the core merging dynamics and the repartitioning of the viscous heating [*Ke and Solomatov*, 2009; *Samuel et al*., 2010; *Monteux et al*., 2011, 2013]. Qualitatively, as the metallic diapir sinks, shear heating occurs at the interface of the diapir and the surroundings [*Samuel et al*., 2010; *Monteux et al*., 2011], leading to the temperature increase of both the diapir and the surrounding mantle. Depending on the effective viscosity contrast between the metallic diapir and the mantle, the mean temperature of the diapir sinking in a Mars-size planet can increase by a few hundred Kelvins [*Monteux et al*., 2009]. This temperature increase is maximal when the diapir and the surrounding mantle are isoviscous [*Monteux et al*., 2009]. The viscosity contrast between molten iron and mantle under Martian conditions may exceed 10–20 orders of magnitude, depending on the mantle temperature. Such viscosity variations are impossible to resolve with our numerical method. However, experiments show that the dynamic influence of these large viscosity variations on diapir sinking is similar to viscosity variations of order 10^2 [*Jellinek et al*., 2003; *Thayalan et al*., 2006], the effects of which we can explore parametrically.

To characterize the influence of a variable viscosity, we monitor the thermochemical readjustment following a 750 km diameter impact and the subsequent core merging for three viscosity models: isoviscous, *T-P* dependent and *T-P* melt dependent. During the impactor's core sinking the viscous heating enhances the temperature and decreases the viscosity of the material immediately surrounding the diapir. The viscosity decrease is mainly localized in the sinking channel where the highest temperatures are reached. In this region, the temperature of the already impact-heated mantle beneath the segregation zone can exceed the solidus temperature and lead to partial melting and a significant viscosity decrease. For the *T-P* melt-dependent viscosity model (Figure 8, third row) and using a reference viscosity $\eta_0 = 10^{21}$ Pa s, the core merging is much faster than for the isoviscous model and occurs in less than 1 kyr when the viscosity contrast is 1000 between the hottest and the coldest material (see Table 3 for values). The spreading of the hot silicate mantle beneath the lithosphere is also facilitated by the increasing viscosity contrast. However, it is achieved within a much longer timescale that is governed by the surrounding mantle viscosity.

The radial deformation of the mantle in the isoviscous case scales with the size of the diapir [e.g., *Morris*, 1982; *Jellinek et al*., 2003; *Thayalan et al*., 2006], whereas in the temperature-dependent case the deformation is confined to the hottest, lowest viscosity material surrounding the diapir with a length scale typically ≈ 0.1 R_{Fe}. Moreover, the horizontal shear stress in the boundary layer between the diapir and the CMB that retards the sinking of the diapir is very small for the *T-P* and *T-P* melt-dependent viscosity. Both these effects increase the sinking velocity when increasing the viscosity contrast between the diapir and the surrounding mantle. Figure 9 shows the evolution of the gap thickness for three viscosity models, isoviscous (with $\eta_0 = 10^{21}$ Pa s), *T-P* dependent (with $c_Z = 10$ and $c_T = 10$–1000), and *T-P* melt dependent (with $c_Z = 10$, $c_1 = 10$–1000, and $c_2 = 30$–3000). The highest viscosity contrasts between the hot diapir and the surrounding mantle are obtained in the *T-P* melt-dependent viscosity model (Figure 8); hence, the coalescence time is shortest (see Figure 6, right).

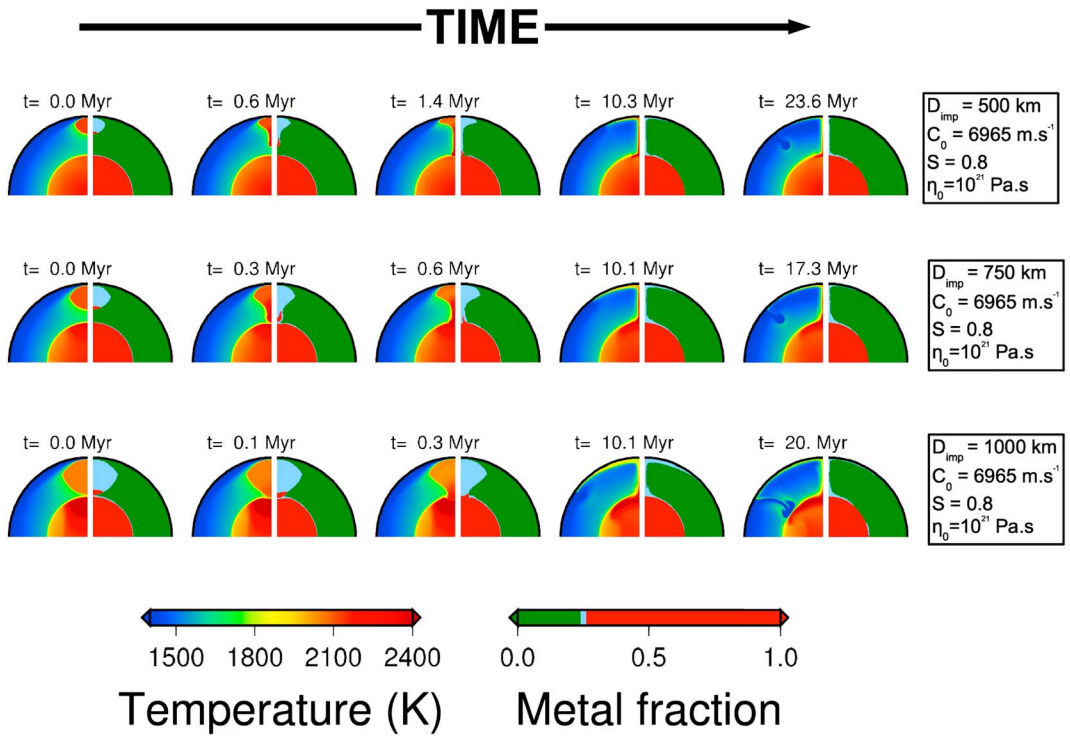

Figure 8. Thermochemical readjustment as a function of time for an isoviscous, a *T-P* dependent (with a viscosity contrast of 100) and a *T-P* melt-dependent (with a viscosity contrast of 100 to 300) viscosity models. (rows 2 and 3) The right part of each panel shows the evolution of the viscosity during the core merging process.

Figure 6 summarizes the influence of the viscosity contrast on the merging times (right) and the temperature of the merging diapir (left) (see values in Table 3). This figure emphasizes the weak influence of the viscosity contrast on the temperature of the impactor's core before merging with the Martian core. The temperature ranges between 2280 and 2330 K while the viscosity contrast increases by 3 orders of magnitude. As detailed above and illustrated in Figure 6 (left) the merging temperature is much more sensitive to the impactor size, while the viscosity contrast is a key parameter when considering the merging time. Figure 6 (right) shows that an increase of the viscosity contrast by 3 orders of magnitude decreases the merging time from 0.36 Myr to ≈ 1 kyr. Here the influence of the impactor size is weaker according to the results of our models.

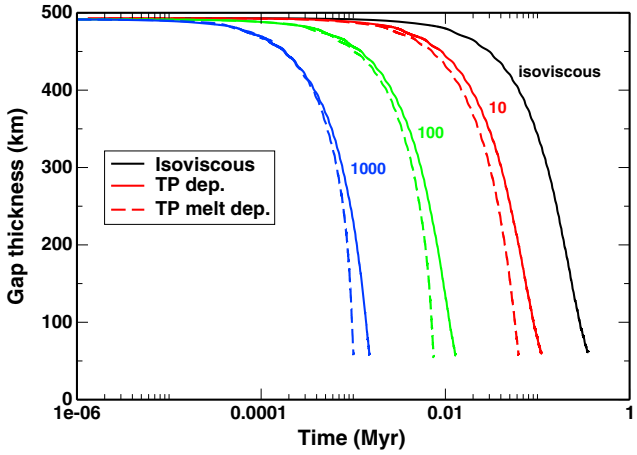

Figure 9. Gap thickness evolution for three different viscosities: uniform (black solid line), *T-P* dependent (colored solid lines), and *T-P* melt dependent (colored dashed lines). For *T-P* and *T-P* melt-dependent viscosities, three viscosity contrasts are represented: 10 (red), 100 (green), and 1000 (blue).

8. Thermochemical Consequences of the Core Merging

This section addresses the consequences of the core merging in terms of thermochemical equilibration.

8.1. The Core-Mantle Equilibrium

After the impact and the formation of the segregation volume, mechanical mixing due to segregation of iron occurs within the partially molten region and can enhance thermochemical equilibrium between the iron from the impactor and molten silicates. The degree of

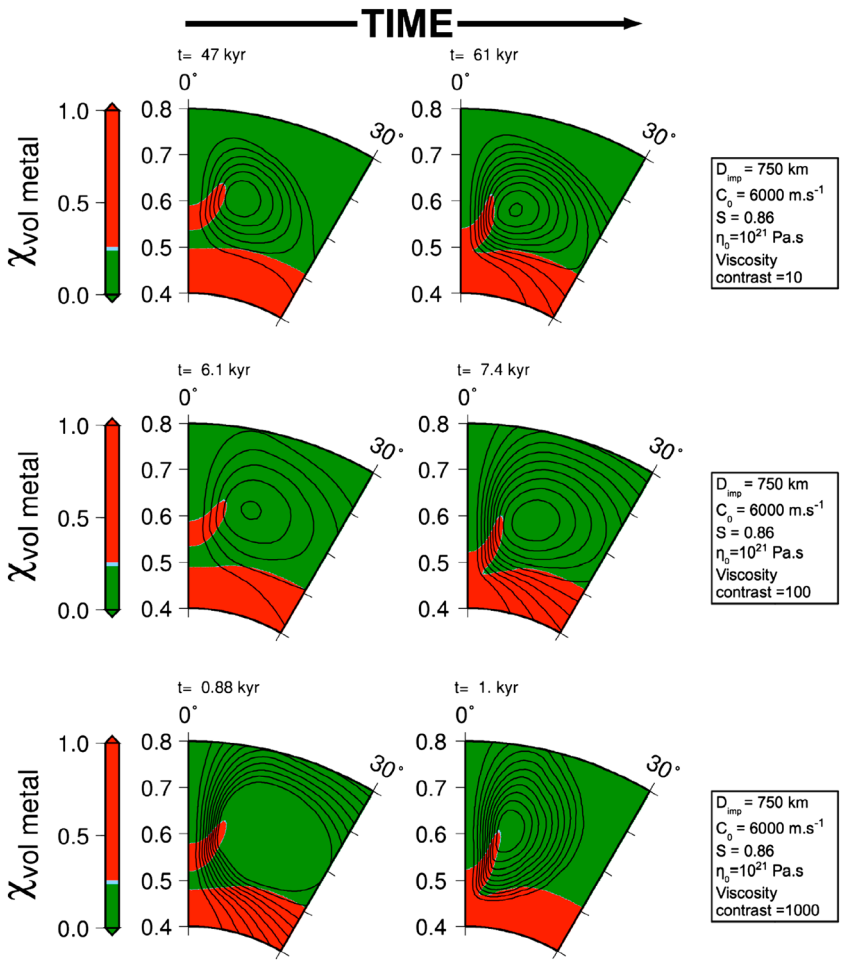

Figure 10. (left to right) Close-up view of the time evolution of the compositional field within the core merging area using the *T-P* melt viscosity model with a viscosity contrast of (top) 10, (middle) 100, and (bottom) 1000. Solid lines represent the streamlines in the reference frame of Mars.

equilibration decreases with increasing characteristic size of the metallic diapirs [*Ulvrová et al.*, 2011; *Deguen et al.*, 2011; *Samuel*, 2012]. For centimeter-sized droplets sinking through a turbulent magma ocean, the thermochemical equilibration is efficient and rapidly achieved [*Samuel*, 2012]. However, during the core merging, the metallic phase may sink as blobs and lead to metal/silicate disequilibrium [*Dahl and Stevenson*, 2010; *Kleine and Rudge*, 2011]. In our models, the impactor's metallic phase is sinking as a large single diapir and chemical equilibrium should depend on the complexity of the flow structure within and outside the diapir [*Ulvrová et al.*, 2011]. However, from the sinking times obtained in our models ($<$ 1 kyr for the most realistic viscosity contrast) (see Table 3), it seems difficult to envision any chemical reequilibration during the diapir sinking. As detailed above, increasing the viscosity contrast between the hot sinking diapir and the surrounding material drastically reduce the merging time but also leads to an elongation of merging core's tail because of the large-scale mantle flow and of the increase in the ability of the diapir to deform (Figure 10). If any chemical equilibration might occur, this thin tail is a good candidate.

The flow induced in the mantle during the sinking can also lead to some entrainment of the silicates from the upper to the lower mantle. This entrainment increases with the diapir size (i.e., with the impactor size) and with the viscosity contrast between the metallic diapir and the mantle (Figure 10). Once the two cores have fully merged, the flow induced by the thermal readjustment within the mantle tends to bring the deep silicate material upward. The accuracy of this phenomenon increases as the viscosity contrast between the diapir and the silicates increases (Figure 10). However, according to the streamlines shown in Figure 10 (right column) the molten silicate material entrained downward during the diapir sinking does not seem to be

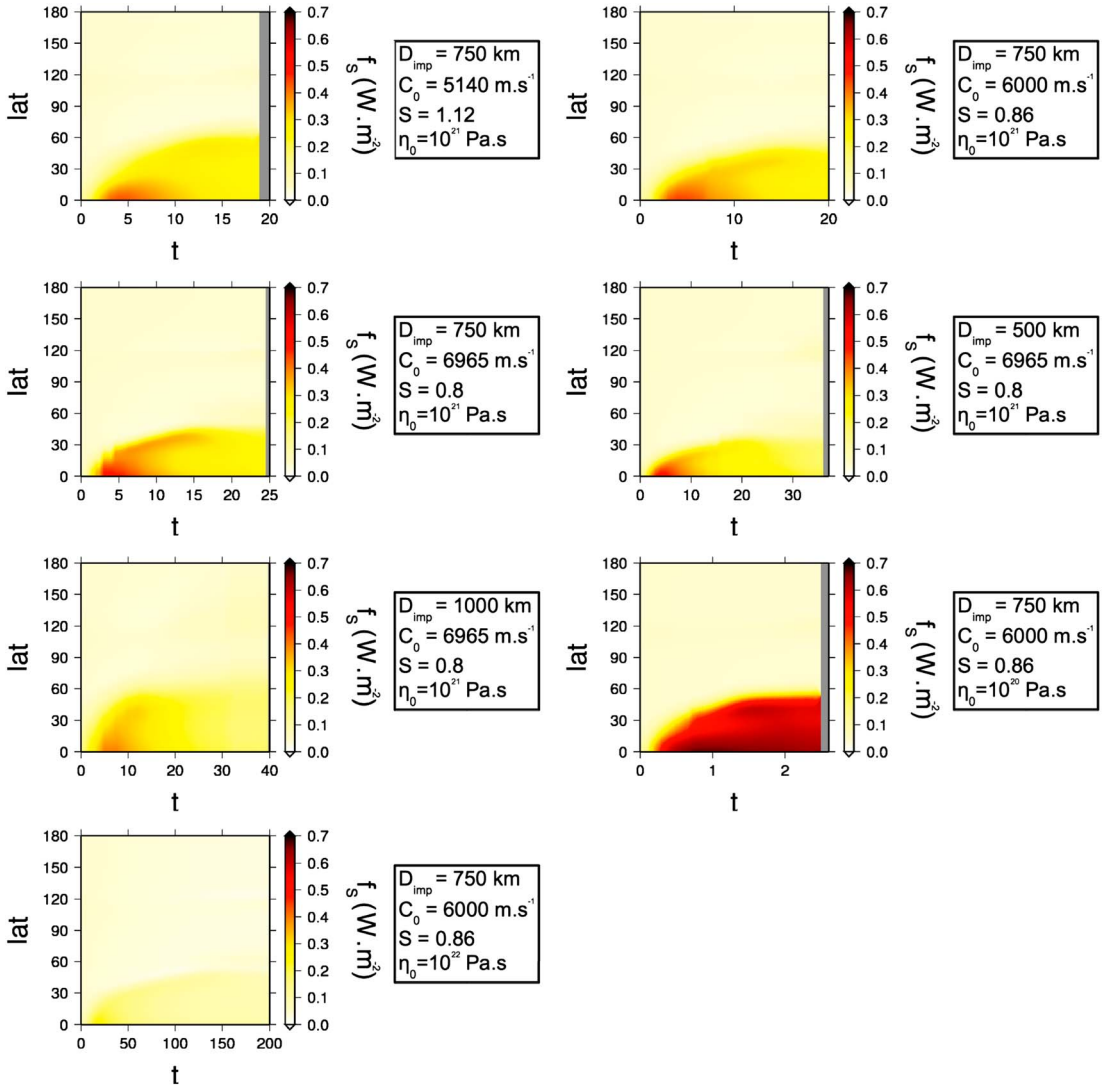

Figure 11. Surface heat flux as a function of time and latitude for different impact properties and average viscosities.

reentrained upward after the merging. Hence, core merging subsequent to a giant impact results in the mixing of silicate material in the mantle.

8.2. Consequences for the Martian Cooling

8.2.1. Mantle Cooling

The impact heating and the viscous dissipation associated with the impactor's core sinking modify the thermal state of the Martian mantle. During and after the merging, a thermal readjustment occurs in the mantle modifying the surface heat flux. The readjustment of the postimpact thermal anomaly within the mantle and its spreading beneath the Martian lithosphere leads to an increase of the surface heat flux. During the early advective stage, corresponding to the flattening of the hot mantle anomaly, the radial extent of the high heat flux patch increases with time. This early advective stage is followed by a later stage of motionless diffusive cooling where the surface heat flux progressively decreases and the mantle thermal anomaly diminishes [*Monteux et al.*, 2007]. The radial extent of the thermal anomaly, its thickness and the duration of the advective stage are strongly dependent on the size of the thermal anomaly and on the physical properties of the planet. Figure 11 shows the time evolution of the surface heat flux (f_S), as a function of the colatitude for different C_0, S, D_{imp}, and η_0 models. Low viscosities and large thermal anomalies favor the spreading of the anomaly over large distances. Hence, the largest sizes for theses patches ($\theta \approx 60°$) are reached for small

viscosities ($\eta_0 = 10^{20}$ Pa s) and large impactor sizes ($D_{imp} = 1000$ km). The time of the transition between the advective and the diffusive stages strongly depends on the mantle viscosity. For $\eta_0 = 10^{21}$ Pa s this time is typically on the order of 10 Myr which is comparable with the models from *Monteux et al.* [2007].

T-P and *T-P* melt-dependent viscosities also influence the evolution of the surface heat flux. Large viscosity contrasts between the hot anomaly and the relatively colder mantle enable easier spreading of the anomaly below the surface [*Koch and Koch*, 1995; *Monteux et al.*, 2007]. As the resistance to internal shearing decreases with increasing viscosity contrast, the horizontal velocity becomes more significant for low viscosities. As a result, for the *T-P* and *T-P* melt-dependent viscosity models, the radial extent increases by ≈ 10%, while the advection time decreases by a factor of ≈ 2 compared to the isoviscous models [*Monteux et al.*, 2007]. Long-term monitoring of the surface heat flux can be very time consuming especially when considering large viscosity contrasts. Hence, we did not monitor the long-term surface heat flux in the nonuniform viscosity cases. However, the temperature dependence of the viscosity should affect our results by a minor amount because the readjustment is mostly controlled by the viscosity far from the segregation volume.

8.2.2. Core Cooling

During the sinking, viscous heating leads to a temperature increase in both the diapir and the surrounding mantle. For a uniform viscosity and for diapir larger than ≈ 70 km in diameter, viscous coupling between the metallic diapir and the surrounding material occurs and a fraction of the gravitational energy of the diapir is converted to heat up the diapir [*Monteux et al.*, 2009]. However, when the diapir is less viscous than the mantle, viscous heating is restricted to the surrounding mantle and is concentrated at the diapir's poles where strain rates are greatest [*Samuel et al.*, 2010; *Monteux et al.*, 2011]. In this case, the temperature of the impactor's core does not increase significantly during the sinking and remains close to its initial presinking temperature at the base of the segregation zone [*Monteux et al.*, 2009].

The temperature of the diapir when merging with the Martian core is also dependent on the distance traveled during the sinking and increases with the initial distance between the diapir (i.e., the initial depth of the segregation zone) and the CMB [*Monteux et al.*, 2009]. Hence, the merging temperature of the diapir may be larger or smaller than the core temperature, depending on the size of the diapir, the distance traveled by the diapir, and the viscosity contrast with the surrounding mantle. For instance, when the segregation volume is large (Figure 5, first row and Figure 7, third row), the initial distance between the diapir and the CMB is not large enough for the diapir to heat up significantly, and the merging diapir is colder than the Martian core. For other sets of parameters the merging core is hotter than the Martian core (Table 3).

Following the merging, the impactor's core is trapped between the hot impacted core material and the hot mantle material from the channel where the diapir has sunk. The positive buoyancy of these two materials between which the impactor's core is trapped tends to spread the impactor's core beneath the CMB (Figure 12). However, the mixing dynamics that occurs within the Martian core after the merging has to be considered here with caution. The injection of a large volume of molten iron of the impactor in a rotating core of the planet is a process that involves Coriolis and inertial forces that are neglected here, because of our infinite Prandtl number approximation. We address this issue in section 10.

9. Effects on the Core Dynamo

A giant impact not only excavates the near surface and heats the upper mantle of a planet as discussed above but also heats the core of the planet in two distinct stages. In the first stage, the shock wave created by the impact propagates in the core, heating it differentially within about 1 h. In the second stage, the merging of the impactor iron diapir modifies the thermal state of the planet's core. Here we investigate the effects of these two stages on the core dynamo of Mars.

The first stage has been studied by many investigators [e.g., *Arkani-Hamed and Olson*, 2010a, 2010b; *Ghods and Arkani-Hamed*, 2011]. Here we follow the procedure adopted by *Arkani-Hamed and Olson* [2010b]. Briefly, the shock wave leads to a temperature increase within the core of the planet, much stronger in the region directly beneath the impact site (Figure 2, bottom left). The low-viscosity rotating liquid core cannot sustain lateral variations of temperature and the core overturns, resulting in a stably stratified temperature which increases with radius. The thermal stratification diminishes the possible preexisting core convection, hence the core dynamo, within a few kyr [*Arkani-Hamed and Olson*, 2010a]. Here we assume it occurs immediately after the impact. Shortly after, the juxtaposition of the superheated stratified core to the relatively colder

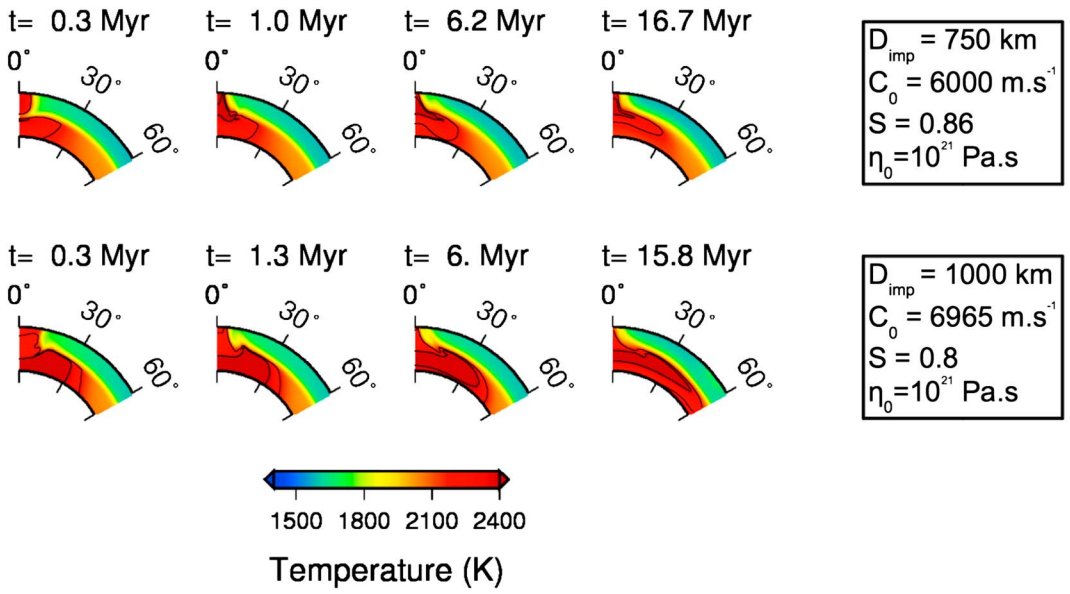

Figure 12. Close-up view of the temperature field within the core merging area for two impactor sizes, two sets of C_0 and S, and viscosity of 10^{21} Pa s.

mantle results in convection in the outer part of the core which generates a dynamo as it thickens over time. Here we first present the results for our reference model ($D_{\mathrm{imp}} = 750$ km, $C_0 = 6000$ m s^{-1}, $S = 0.86$ and $\eta = 10^{21}$ Pa s) in some detail and then provide the major results for the other models.

Included in Figure 2 (bottom left) is the impact-induced temperature increase inside our reference model, showing the differentially heated mantle and core. We note that the temperature in the uppermost part of the core directly beneath the impact site is higher than that in the adjacent mantle. This is partly due to shock pressure jump as the shock wave inters the core and partly because of low-specific heat of the iron core, 600 J/kg/K, compared to that of the silicate mantle, 1200 J/kg/K. Also, the impact heating of the core is appreciable only within ~40° colatitude relative to the symmetric axis passing the impact site and the center of the planet, the area which covers only 12% of the core's surface. About 88% of the core is juxtaposed to the base of the mantle with preimpact temperature. Once the core stratifies and the hottest part of the core is placed directly beneath the core-mantle boundary, the core essentially cools almost globally. The thermal evolution of the core is calculated by numerically solving the 1-D enthalpy equation and following the procedure adopted by *Arkani-Hamed and Olson* [2010b]. The radial grid interval is taken to be 100 m to allow accurate determination of the thickness of the thermal boundary layer in the convecting outer core. The domain of calculation includes the entire core plus a 100 km thick thermal boundary layer at the base of the mantle. The preimpact temperature is assumed adiabatic inside the core with 2000 K at the core-mantle boundary. It linearly decreases in the overlying mantle layer to 1500 K at the top of the layer. The spherically symmetric temperature distribution inside the core immediately after the impact is obtained by first adding the preimpact temperature to the impact-induced temperature increase and then allowing the thermal stratification. The liquid core has a kinetic viscosity of 10^4 m^2/s and it rotates with a 24 h period (see Table 2 for physical properties of the core). The core viscosity must be much smaller. However, reducing the viscosity by 8 orders of magnitude has only minor effects on the core cooling [*Arkani-Hamed and Olson*, 2010b], because the core cooling is mainly controlled by the overlying solid mantle.

To illustrate the effects of the impactor core merging on the Martian core dynamo two scenarios are calculated for each models listed in Table 3: one without considering the merging and the other with merging. Figure 13 shows the thermal evolution of the core and the overlying mantle for 300 Myr after the impact where no merging is considered. The positive temperature gradient deep in the core retains stable condition, prohibiting convection, while the upper most part of the core convects and maintains adiabatic temperature as it thickens and penetrates to deeper parts of the core. Although the very high temperature at the top of the stratified core diminishes rapidly, the impact heating remains appreciable for much longer time. Figure 14 shows the time variations of the thickness of the convecting outer core, the heat flux at the core-mantle boundary, the magnetic

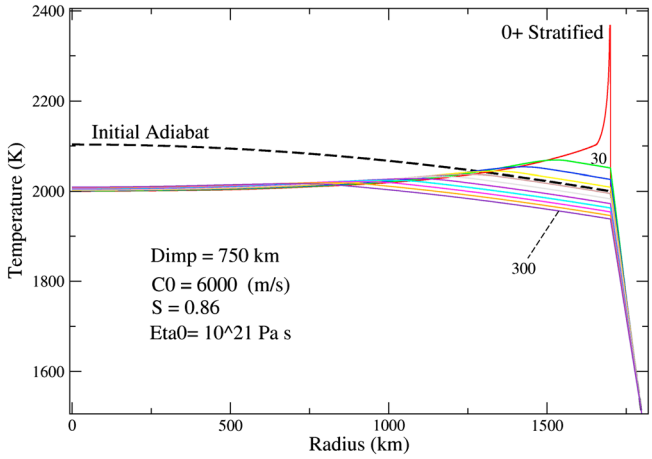

Figure 13. Thermal evolution of Martian core after an impact, where no core merging is considered. The temperature is shown at 30 Myr intervals. The numbers on the curves denote time after the impact in Myr. The curve "Initial Adiabat" is the preimpact temperature, and "0+ Stratified" denotes the temperature after the first stage of stratification. D_{imp} is the impactor diameter in kilometer, C_0 is the acoustic velocity of the mantle in m/s, S is the constant in the EOS, and η_0 is the mantle viscosity assumed isoviscous mantle.

Reynolds number and the mean magnetic intensity inside the convecting outer core for 300 Myr after the impact. Similar to the results obtained by other investigator [e.g., *Arkani-Hamed and Olson*, 2010b; *Arkani-Hamed and Ghods*, 2011], the impact certainly cripples the possible preimpact core dynamo and it takes around 150–200 Myr for the convecting outer core to generate a strong core dynamo, taking the threshold value of 20 for the magnetic Reynolds number. We note that the outer core is not thick enough to generate an appreciable dynamo within the first ~20 Myr after the impact, despite very high heat flux at the core-mantle boundary.

Due to the positive buoyancy relative to the core of Mars, the impactor diapir spreads on the core (Figure 12) and creates a super-heated iron layer of ~0.8 km thickness. Figure 15 compares the thermal evolution of the core for the first 10 Myr with and without the diapir merging. At the time of merging the iron diapir is about 100 K hotter than the uppermost part of Mars' core. However, the iron layer cools very rapidly such that the difference between the two models almost disappears within less than 2 Myr. This is better illustrated in Figure 16 where the thickness of the convecting outer core, the heat flux at the core-mantle boundary, and the magnetic Reynolds number and the mean magnetic field intensity of the convecting outer core are displayed within the first 1 Myr after the impact for both models. The merging iron layer reinitiates convection at about 0.37 Myr, and its effects diminish rapidly within the first 1 Myr.

The effects of physical parameters of the mantle and the size of the impactor are also estimated for both scenarios, with and without merging. Figures 17 and 18 show the effects of the diapir merging on the core dynamo for different viscosity models of the mantle, different C_0 and S values as well as different size of the impactor. The

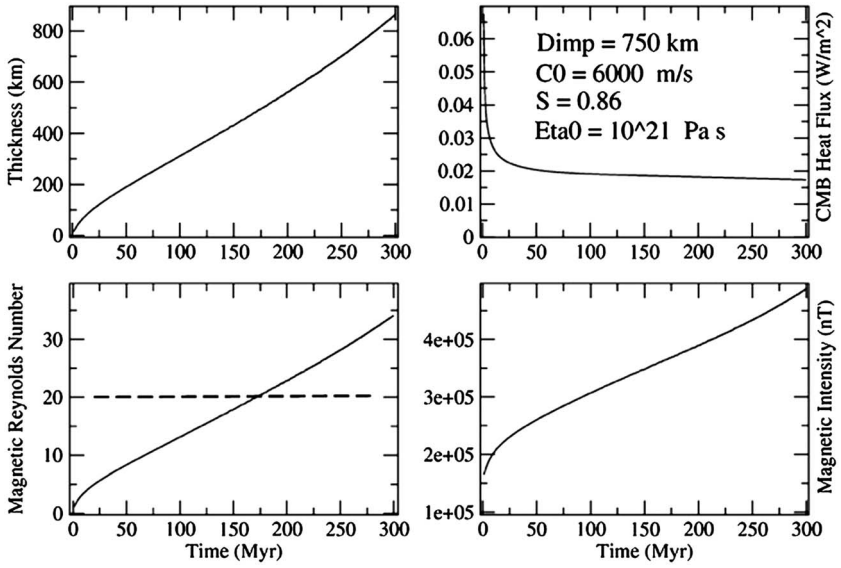

Figure 14. The evolution of the thickness of the convecting outer core, the heat flux at the core-mantle boundary, the magnetic Reynolds number, and the mean magnetic intensity in the convecting zone corresponding to the thermal evolution of the core shown in Figure 13.

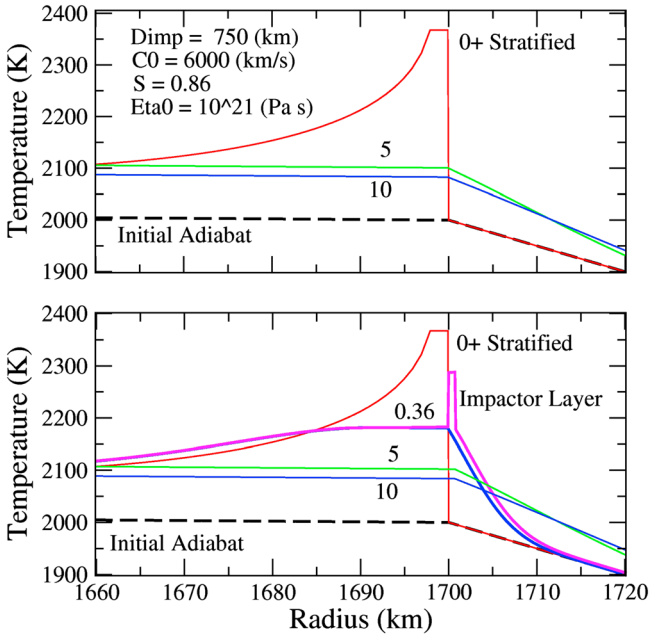

Figure 15. Thermal evolution of Martian core within 10 Myr after an impact. (top) With no core merging and (bottom) with core merging that occurs at 0.36 Myr after the impact. The blue and magenta curves in Figure 15 (bottom) show the temperature distribution immediately before and immediately after the core merging. See Figure 13 for details.

isoviscous mantle with a viscosity of 10^{22} Pa s, and to a lesser extent 10^{21} Pa s, delays the merging time and has appreciable effects on the dynamo. It takes longer time for the iron diapir of the smaller impactor ($D_{imp} = 500$ km), which initiates at the base of a smaller segregation zone, to sink through the mantle before merging to the core, hence has appreciable effect on the core dynamo because the Martian core cools prior to the merging. The $C_0 = 6965$ (m/s) and $S = 0.8$ model results in an appreciable merging effects. However, the effects diminish within a few Myr in all models. It is plausible to conclude that the main effect of an impact on the core dynamo is due to direct heating of the core (see Figure 14), which was not considered by *Monteux et al.* [2013], and diapir merging has almost negligible effects. This is largely because the iron layers produced on the Martian core by the diapirs are very thin, and no dynamo can be generated inside the layers. It requires a thickness of about 30 km for an iron layer to generate dynamo [e.g., *Reese and Solomatov*, 2010]. The iron layers can only delay the initiation of the dynamo for a very short time.

10. Limitations of Our Models

The stratification of the differentially heated Martian core occurs while the impactor's core diapir is still descending in the mantle. The core merging incorporates some new material within the Martian core with a

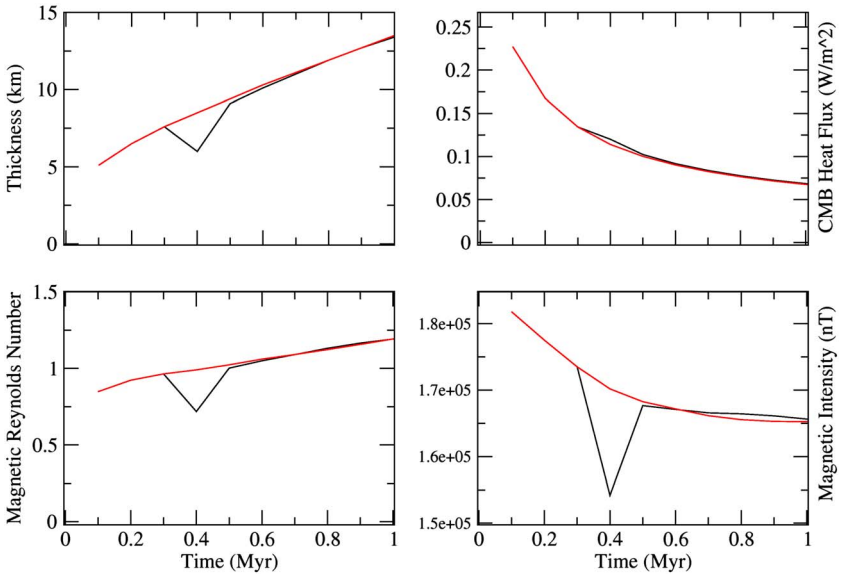

Figure 16. The evolution of the thickness of the convecting outer core, the heat flux at the core-mantle boundary, the magnetic Reynolds number, and the mean magnetic intensity in the convecting zone within the first 1 Myr. The red curves are for the no merging scenario, and the black ones are for the merging scenario.

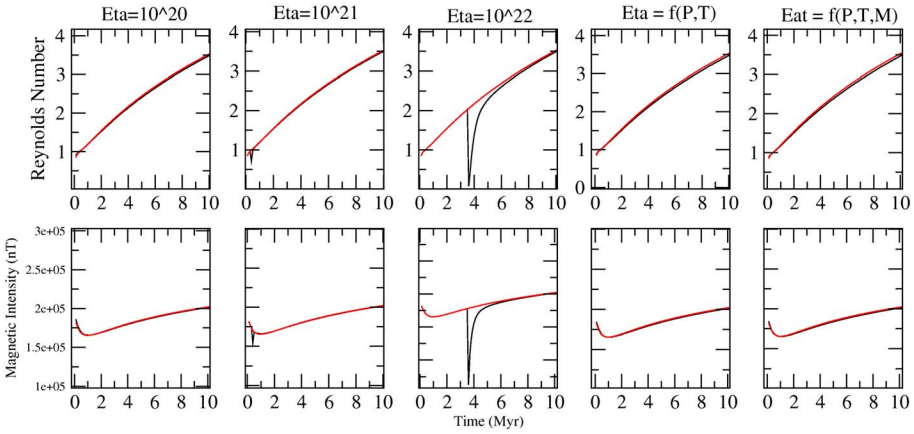

Figure 17. Effects of the mantle viscosity on the Reynolds number and the mean magnetic intensity in the convecting outer core for a model with 750 km impactor diameter, $C_0 = 6000$ m/s, and $S = 0.86$. *Eta* at the top denotes the mantle viscosity: either isoviscous with 10^{20}, 10^{21}, or 10^{22} Pa s, or temperature- and pressure-dependent (f(*P*,*T*)), or temperature, pressure, and melt dependent (f(*P*, *T*, *M*)) with a viscosity contrast of 1000. The red curves are for the no merging scenario, and the black ones are for the merging scenario.

temperature that depends on the size of the impactor, the segregation volume and the viscosity contrast between the diapir and the mantle. In any case, the core merging leads to lateral temperature variations and may initiate restratification of the core.

Our present numerical model of spreading the iron diapir on the Martian core does not include the rotation effect (i.e., no Coriolis forces) and assumes an infinite Prandtl number (i.e., no inertial forces) in the momentum equation. Hence, we do not obtain the stratification that likely occurs immediately after the impact as discussed in the previous section, and the second restratification that would occur after the complete core merging. Consequently, materials from our lowest viscosity and largest diapir spread beneath the CMB as a thin, axisymmetric gravity current (see Figure 12). The spreading of the hot core anomaly stops when diffusive cooling overcomes advective transport leading to a partial stratification of the core [*Monteux et al.*, 2013]. This thermal stratification persists until the thermal anomaly introduced by the gravity current diffuses into the overlying mantle and the underlying part of the core. The dynamics of thermal mixing under realistic core viscosities will be the subject of a separated study.

11. Conclusions

Giant impacts may have significantly influenced the mantle dynamics of Mars. We investigated the postimpact thermochemical readjustment after one single giant impact occurring during the early stages of

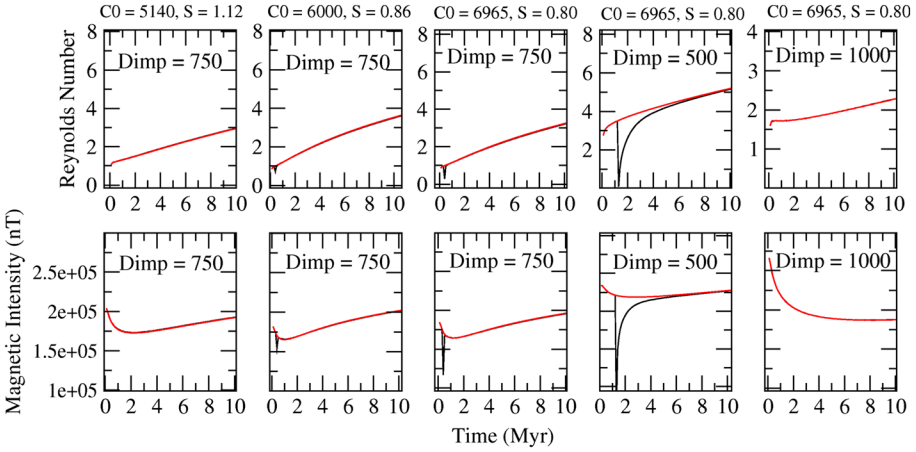

Figure 18. Effects of the acoustic velocity, C_0, and EOS constant, *S*, of the mantle on the magnetic Reynolds number and mean magnetic intensity of the convecting outer core. The mantle has a constant viscosity of 10^{21} Pa s. *D* denotes the impactor diameter in kilometer. The red curves are for the no merging scenario, and the black ones are for the merging scenario.

the Martian history. In particular, we studied the thermal consequences of the sinking of an impactor's core in the Martian mantle as a function of the impactor size and for different mantle viscosity models. Our results show that the core merging is a fast process that occurs in a time mainly governed by the mantle viscosity. Although this study is the continuation of the study by *Monteux et al*. [2013], several improvements have been achieved in the characterization of the impact heating, the initial postimpact geometry of the impactor's core and the viscosity models. Indeed, from our results we can now separate the influences of the impactor size (D_{imp}), the ability of the impacted mantle to be shock heated (C_0 and S) and the mantle viscosity (type and viscosity contrast) on the time required for sinking and on the temperature of the impactor's core when merging with the Martian one. We can now conclude that the viscosity does not play a key role in the thermal evolution during the merging (only modifying the merging temperature by ≈ 1 % for the range of viscosities adopted here). However, it plays an important role on the sinking time which is very sensitive to the viscosity contrast between the sinking diapir and the surrounding material that can decrease from 0.3 Myr to 1 kyr. From the range of parameters considered here (with viscosity contrast up to 3 orders of magnitude), the merging time is probably too short to envision any chemical equilibration during the sinking. Concerning the thermal evolution, the impactor diameter D_{imp} and the (C_0, S) values seem to be the key parameters that govern both the merging time (by controlling the diapir size and initial depth) and the merging temperature that can vary by 10% in the range of parameters studied here (from 2130 to 2350 K). In our models, we assume that the impact occurs with a moderate impact velocity (about twice the Martian escape velocity); larger impact velocities can substantially increase the postimpact temperature in the merging core prior to its sinking which strengthen the importance of the impact parameters on the merging temperature.

Our study also highlights that, even if the core merging processes could reduce the efficiency of chemical equilibration during the core formation in terrestrial planets [*Kleine and Rudge*, 2011], the flow dynamics generated within the mantle during the merging process for large viscosity contrasts could enhance some mixing between upper and deep silicate material even in the absence of mantle convection. Because the characteristic timescales of thermal readjustment within the mantle are long, the hot postimpact mantle anomaly creates a surface heat flux anomaly as it spreads below the Martian surface. The spreading stage lasts ≈ 10 Myr and is followed by a diffusive cooling that occurs within a longer timescale. More importantly, we can now make a better estimate of the influence of the core merging process on the Martian dynamo. The main effect of a large impact on the core dynamo is due to direct heating of the core, and diapir merging has almost negligible effects. The spreading of the merging diapir as a hot and thin layer surrounding the preexisting Martian core can only delay the initiation of the dynamo for a very short time.

In our models, the impact angle is vertical which maximizes the postimpact melt volume, hence the segregation volume in which the metal/silicates separation occurs [*Pierazzo and Melosh*, 2000]. Oblique impacts could influence the core merging dynamics by reducing the initial position of the metallic diapir and modifying the shape of the postimpact mantle thermal anomaly. The asymmetry introduced in the thermal state of the mantle by an oblique impact cannot be included in our current axisymmetric model and has to be modeled in a 3-D model in the future. However, an oblique impact has less effect on the cessation and reactivation of the core dynamo, except for the amount of impact heating of the core. This is because the core stratifies almost immediately after the impact and retains a spherically symmetric temperature distribution.

Acknowledgments

J.M. is funded by Agence Nationale de la Recherche (Accretis decision ANR-10-PDOC-001-01), and J.A.H. is supported by the Natural Sciences and Engineering Research Council (NSERC) of Canada. We also thank the two anonymous reviewers and the Associate Editor for valuable comments, which helped to improve the manuscript significantly.

References

Ahrens, T. J., and M. L. Johnson (1995), Shock wave data for rocks, in *Mineral Physics and Crystallography, A Handbook of Physical Constants*, vol. 3, edited by T. J. Ahrens, pp. 35–44, Amer. Geophys. Union, Washington, D. C.

Ahrens, T. J., and J. D. O'Keefe (1987), Impact on the Earth, ocean and atmosphere, *Int. J. Impact Eng.*, *5*, 13–32.

Andrews-Hanna, J. C., M. T. Zuber, and W. B. Banerdt (2008), The Borealis basin and the origin of the Martian crustal dichotomy, *Nature*, *453*, 1212–1215, doi:10.1038/nature07011.

Arkani-Hamed, J., and A. Ghods (2011), Could giant impacts cripple core dynamos of small terrestrial planets?, *Icarus*, *212*, 920–934.

Arkani-Hamed, J. (2005), Magnetic crust of Mars, *J. Geophys. Res.*, *110*, E08005, doi:10.1029/2004JE002397.

Arkani-Hamed, J. (2012), Life of the Martian dynamo, *Phys. Earth Planet. Inter.*, *196-197*, 83–96.

Arkani-Hamed, J., and P. Olson (2010a), Giant impact stratification of the Martian core, *Geophys. Res. Lett.*, *370*, L02201, doi:10.1029/2009GL041417.

Arkani-Hamed, J., and P. Olson (2010b), Giant impacts, core stratification, and failure of the Martian dynamo, *J. Geophys. Res.*, *115*, E07012, doi:10.1029/2010JE003579.

Asphaug, E. (2010), Similar-sized collisions and the diversity of planets, *Chemie der Erde / Geochem.*, *70*, 199–219, doi:10.1016/j.chemer.2010.01.004.

Bagdassarov, N., G. Solferino, G. J. Golabek, and M. W. Schmidt (2009), Centrifuge assisted percolation of Fe–S melts in partially molten peridotite: Time constraints for planetary core formation, *Earth Planet. Sci. Lett.*, *288*(1–2), 84–95, doi:10.1016/j.epsl.2009.09.010.

Batchelor, G. (1967), *An Introduction to Fluid Dynamics*, Cambridge Univ. Press, Cambridge, U. K.
Benz, W., W. L. Slattery, and A. G. W. Cameron (1988), Collisional stripping of Mercury's mantle, *Icarus*, *74*, 516–528, doi:10.1016/0019-1035(88)90118-2.
Bills, B. G., G. A. Neumann, D. E. Smith, and M. T. Zuber (2005), Improved estimate of tidal dissipation within Mars from MOLA observations of the shadow of Phobos, *J. Geophys. Res.*, *110*, E07004, doi:10.1029/2004JE002376.
Breuer, D., S. Labrosse, and T. Spohn (2010), Thermal evolution and magnetic field generation in terrestrial planets and satellites, *Space Sci. Rev.*, *152*, 449–500.
Cameron, A. G. W., and W. Benz (1991), The origin of the Moon and the single impact hypothesis IV, *Icarus*, *92*, 204–216.
Canup, R. M. (2004), Simulations of a late lunar-forming impact, *Icarus*, *168*, 433–456, doi:10.1016/j.icarus.2003.09.028.
Chambers, J. E. (2004), Planetary accretion in the inner solar system, *Earth Planet. Sci. Lett.*, *223*, 241–252.
Coradini, A., C. Federico, and P. Lanciano (1983), Earth and Mars—Early thermal profiles, *Phys. Earth Planet. Inter.*, *31*, 145–160.
Croft, S. K. (1982), A first-order estimate of shock heating and vaporization in oceanic impacts, in *Geological Implications of Impacts of Large Asteroids and Comets on Earth*, vol. 190, edited by T. L. Silver and P. H. Schultz, pp. 143–152, *Spec. Pap. Geol. Soc. Am.*, Boulder, Colo.
Dahl, T. W., and D. J. Stevenson (2010), Turbulent mixing of metal and silicate during planet accretion and interpretation of the Hf-W chronometer, *Earth Planet. Sci. Lett.*, *295*, 177–186.
Dauphas, N., and A. Pourmand (2011), Hf-W-Th evidence for rapid growth of Mars and its status as a planetary embryo, *Nature*, *473*, 489–493.
Davies, G. F. (1982), Ultimate strength of solids and formation of planetary cores, *Geophys. Res. Lett.*, *9*, 1267–1270.
Deguen, R., P. Olson, and P. Cardin (2011), Experiments on turbulent metal–silicate mixing in a magma ocean, *Earth Planet. Sci. Lett.*, *310*, 303–313.
Douglas, J. (1955), On the numerical integration of $\partial^2 u/\partial x^2 + \partial^2 u/\partial y^2 = \partial u/\partial t$ by implicit methods, *J. Soc. Ind. Appl. Math.*, *3*, 42–65, doi:10.1137/0103004.
Dziewonski, A. M., and D. L. Anderson (1981), Preliminary reference Earth model, *Phys. Earth Planet. Inter.*, *25*, 297–356.
Frey, H. V., J. H. Roark, K. M. Shockey, E. L. Frey, and S. E. H. Sakimoto (2002), Ancient lowlands on Mars, *Geophys. Res. Lett.*, *29*(10), 1384, doi:10.1029/2001GL013832.
Gerya, T. V., and D. A. Yuen (2007), Robust characteristics method for modelling multiphase visco-elastic thermo-mechanical problems, *Phys. Earth Planet. Inter.*, *163*, 83–105.
Ghods, A., and J. Arkani-Hamed (2007), Impact-induced convection as the main mechanism for formation of mare basalts, *J. Geophys. Res.*, *112*, E03005, doi:10.1029/2006JE002709.
Ghods, A., and J. Arkani-Hamed (2011), Effects of the Borealis impact on the mantle dynamics of Mars, *Phys. Earth Planet. Inter.*, *188*, 37–46.
Golabek, G. J., T. V. Gerya, B. J. P. Kaus, R. Ziethe, and P. J. Tackley (2009), Rheological controls on the terrestrial core formation mechanism, *Geochem. Geophys. Geosyst.*, *10*, Q11007, doi:10.1029/2009GC002552.
Hadamard, J. (1911), Mouvement permanent lent d'une sphère liquide et visqueuse dans un liquide visqueux, *C.R. Acad. Sci.*, *152*, 1735–1738.
Hartmann, W. K., and D. R. Davis (1975), Satellite-sized planetesimals and lunar origin, *Icarus*, *24*, 504–514.
Hofmeister, A. M. (1999), Mantle values of thermal conductivity and the geotherm from phonon lifetimes, *Science*, *283*, 1699–1706.
Höink, T., J. Schmalzl, and U. Hansen (2005), Formation of compositional structures by sedimentation in vigorous convection, *Phys. Earth Planet. Inter.*, *153*, 11–20.
Honda, R., H. Mizutani, and T. Yamamoto (1993), Numerical simulation of Earth's core formation, *J. Geophys. Res.*, *98*, 2075–2090.
Jellinek, A. M., H. M. Gonnermann, and M. A. Richards (2003), Plume capture by divergent plate motions: Implications for the distribution of hotspots, geochemistry of mid-ocean ridge basalts, and estimates of the heat flux at the core-mantle boundary, *Earth Planet. Sci. Lett.*, *205*, 361–378, doi:10.1016/S0012-821X(02)01070-1.
Jutzi, M., and E. Asphaug (2011), Forming the lunar farside highlands by accretion of a companion moon, *Nature*, *476*, 69–72.
Katz, R. F., M. Spiegelman, and C. H. Langmuir (2003), A new parameterization of hydrous mantle melting, *Geochem. Geophys. Geosyst.*, *4*(9), 1073, doi:10.1029/2002GC000433.
Ke, Y., and V. S. Solomatov (2009), Coupled core–mantle thermal evolution of early Mars, *J. Geophys. Res.*, *114*, E07004, doi:10.1029/2008JE003291.
Kleine, T., and J. F. Rudge (2011), Chronometry of meteorites and the formation of the Earth and Moon, *Elements*, *7*, 41–46.
Kleine, T., C. Münker, K. Mezger, and H. Palme (2002), Rapid accretion and early core formation on asteroids and the terrestrial planets from Hf–W chronometry, *Nature*, *418*, 952–955.
Koch, D. M., and D. L. Koch (1995), Numerical and theoretical solutions for a drop spreading below a free fluid surface, *J. Fluid Mech.*, *287*, 251–278.
Laney, C. B. (1998), *Computational Gas Dynamics*, Cambridge University Press, Cambridge.
Lee, D. C., and A. N. Halliday (1997), Core formation on Mars and differentiated asteroids, *Nature*, *388*, 854–857.
Louzada, K. L., and S. T. Stewart (2009), Effects of planet curvature and crust on the shock pressure field around impact basins, *Geophys. Res. Lett.*, *36*, L15203, doi:10.1029/2009GL037869.
Marinova, M. M., O. Aharonson, and E. Asphaug (2008), Mega-impact formation of the Mars hemispheric dichotomy, *Nature*, *453*, 1216–1219, doi:10.1038/nature07070.
McGill, G. E., and A. M. Dimitriou (1990), Origin of the Martian global dichotomy by crustal thinning in the Late Noachian or early Hesperian, *J. Geophys. Res.*, *95*, 12,595–12,605.
McQueen, R. G., S. P. Marsh, and J. N. Fritz (1967), Hugoniot equation of state of twelve rocks, *J. Geophys. Res.*, *72*, 4999–5036.
Melosh, H. J. (1989), *Impact Cratering: A Geologic Process*, Oxford Univ. Press, New York.
Mitani, N. K. (2003), Numerical simulations of shock attenuation in solids and reevaluation of scaling law, *J. Geophys. Res.*, *108*(E1), 5003, doi:10.1029/2000JE001472.
Monteux, J., N. Coltice, F. Dubuffet, and Y. Ricard (2007), Thermo-mechanical adjustment after impacts during planetary growth, *Geophys. Res. Lett.*, *34*, L24201, doi:10.1029/2007GL031635.
Monteux, J., Y. Ricard, N. Coltice, F. Dubuffet, and M. Ulvrová (2009), A model of metal-silicate separation on growing planets, *Earth Planet. Sci. Lett.*, *287*, 353–362.
Monteux, J., A. M. Jellinek, and C. L. Johnson (2011), Why might planets and moons have early dynamos?, *Earth Planet. Sci. Lett.*, *310*, 349–359, doi:10.1016/j.epsl.2011.08.014.
Monteux, J., A. M. Jellinek, and C. L. Johnson (2013), Dynamics of core merging after a mega-impact with applications to Mars' early dynamo, *Icarus*, *226*, 20–32.
Morris, S. (1982), The effects of a strongly temperature-dependent viscosity on slow flow past a hot sphere, *J. Fluid Mech.*, *124*, 1–26, doi:10.1017/S0022112082002389.

Neukum, G., and D. V. Wise (1976), Mars: A standard crater curve and possible new time scale, *Science*, *194*, 1381–1387.
Neumann, W., D. Breuer, and T. Spohn (2012), Differentiation and core formation in accreting planetesimals, *Astron. Astrophys.*, *543*, A141, 23.
Nimmo, F., and T. Kleine (2007), How rapidly did Mars accrete? Uncertainties in the Hf/W timing of core formation, *Icarus*, *191*, 497–504, doi:10.1016/j.icarus.2007.05.002.
Nimmo, F., S. D. Hart, D. G. Korycansky, and C. B. Agnor (2008), Implications of an impact origin for the Martian hemispheric dichotomy, *Nature*, *453*, 1220–1223, doi:10.1038/nature07025.
Peaceman, D. W., and H. H. Rachford (1955), The numerical solution of parabolic and elliptic differential equations, *J. Soc. Ind. Appl. Math.*, *3*, 28–41, doi:10.1137/0103003.
Pierazzo, E., and H. J. Melosh (2000), Melt production in oblique impacts, *Icarus*, *145*, 252–261.
Pierazzo, E., A. M. Vickery, and H. J. Melosh (1997), A reevaluation of impact melt production, *Icarus*, *127*, 408–423.
Ratcliff, J. T., P. J. Tackley, G. Schubert, and A. Zebib (1997), Transitions in thermal convection with strongly variable viscosity, *Phys. Earth Planet. Inter.*, *102*, 201–212.
Reese, C. C., and V. S. Solomatov (2006), Fluid dynamics of local Martian magma oceans, *Icarus*, *184*, 102–120.
Reese, C. C., and V. S. Solomatov (2010), Early Martian dynamo generation due to giant impacts, *Icarus*, *207*, 82–97, doi:10.1016/j.icarus.2009.10.016.
Ricard, Y., O. Šrámek, and F. Dubuffet (2009), A multi-phase model of runaway core-mantle segregation in planetary embryos, *Earth Planet. Sci. Lett.*, *284*, 144–150.
Roberts, J. H., and J. Arkani-Hamed (2012), Impact-induced mantle dynamics on Mars, *Icarus*, *218*, 278–289, doi:10.1016/j.icarus.2011.11.038.
Roberts, J. H., and O. S. Barnouin (2012), The effect of the Caloris impact on the mantle dynamics and volcanism of Mercury, *J. Geophys. Res.*, *117*, E02007, doi:10.1029/2011JE003876.
Roberts, J. H., R. J. Lillis, and M. Manga (2009), Giant impacts on early Mars and the cessation of the Martian dynamo, *J. Geophys. Res.*, *114*, E04009, doi:10.1029/2008JE003287.
Roe, P. L. (1986), Characteristic-based schemes for the Euler equations, *Annu. Rev. Fluid Mech.*, *18*, 337–365.
Rubie, D. C., H. J. Melosh, J. E. Reid, C. Liebske, and K. Righter (2003), Mechanisms of metal-silicate equilibration in the terrestrial magma ocean, *Earth Planet. Sci. Lett.*, *205*, 239–255.
Rybczynski, W. (1911), Über die fortschreitende Bewegung einer flüssigen Kugel in einem Medium, *Bull. Acad. Sci. Cracovie*, *1*, 40–46.
Samuel, H. (2012), A re-evaluation of metal diapir breakup and equilibration in terrestrial magma oceans, *Earth Planet. Sci. Lett.*, *313*, 105–114, doi:10.1016/j.epsl.2011.11.001.
Samuel, H., and P. J. Tackley (2008), Dynamics of core formation and equilibration by negative diapirism, *Geochem. Geophys. Geosyst.*, *9*, Q06011, doi:10.1029/2007GC001896.
Samuel, H., P. J. Tackley, and M. Evonuk (2010), Heat partitioning in terrestrial planets during core formation by negative diapirism, *Earth Planet. Sci. Lett.*, *290*, 13–19.
Schubert, G., D. L. Turcotte, and P. Olson (2001), *Mantle convection in the Earth and planets*, Cambridge University Press, New York.
Senshu, H., K. Kuramoto, and T. Matsui (2002), Thermal evolution of a growing Mars, *J. Geophys. Res.*, *107*(E12), 5118, doi:10.1029/2001JE001819.
Shahnas, H., and J. Arkani-Hamed (2007), Viscous and impact demagnetization of Martian crust, *J. Geophys. Res.*, *112*, E02009, doi:10.1029/2005JE002424.
Shannon, M. C., and C. B. Agee (1996), High pressure constraints on percolative core formation, *Geophys. Res. Lett.*, *23*, 2717–2720.
Smith, J. V. (1979), Mineralogy of the planets: A voyage in space and time, *Mineral. Mag.*, *43*, 1–89.
Solomatov, V. S. (2000), Fluid dynamics of a terrestrial magma ocean, in *Origin of the earth and moon*, edited by R. M. Canup et al., pp. 323–338, University of Arizona Press, Tucson.
Solomon, S. C., et al. (2005), New perspectives on ancient Mars, *Science*, *307*, 1214–1220.
Šrámek, O., Y. Ricard, and F. Dubuffet (2010), A multiphase model of core formation, *Geophys. J. Int.*, *181*, 198–220, doi:10.1111/j.1365-246X.2010.04528.x.
Stacey, F. D., and O. L. Anderson (2001), Electrical and thermal conductivities of Fe-Ni-Si alloy under core conditions, *Phys. Earth Planet. Inter.*, *124*, 153–162.
Stevenson, D. J. (1989), Formation and early evolution of the Earth, in *Mantle Convection and Plate Tectonics*, edited by W. R. Peltier, pp. 818–868 Routledge, Abingdon, U. K.
Stevenson, D. J. (1990), Fluid dynamics of core formation, in *Origin of the Earth*, edited by H. E. Newsom and J. H. Jones, pp. 231–249, Oxford Univ, New York.
Stevenson, D. J. (2003), Planetary science: Mission to Earth's core—A modest proposal, *Nature*, *423*, 239–240.
Thayalan, V., A. M. Jellinek, and A. Lenardic (2006), Recycling the lid: Effects of subduction and stirring on boundary layer dynamics in bottom heated planetary mantle convection, *Geophys. Res. Lett.*, *33*, L20318, doi:10.1029/2006GL027668.
Tonks, W. B., and H. J. Melosh (1992), Core formation by giant impacts, *Icarus*, *100*, 326–346.
Tonks, W. B., and H. J. Melosh (1993), Magma ocean formation due to giant impacts, *J. Geophys. Res.*, *98*, 5319–5333.
Trunin, R. F. (2001), Experimental data on shock compression and adiabatic expansion of condensed matter, *Academic Publication*, *RFNC-VNIIEF*, *SAROV*.
Ulvrová, M., N. Coltice, Y. Ricard, S. Labrosse, F. Dubuffet, J. Velímský, and O. Šrámek (2011), Compositional and thermal equilibration of particles, drops, and diapirs in geophysical flows, *Geochem. Geophys. Geosyst.*, *12*, Q10014, doi:10.1029/2011GC003757.
Vocadlo, L., D. Alfè, G. D. Price, and M. J. Gillan (2000), First principles calculations on the diffusivity and viscosity of liquid Fe–S at experimentally accessible conditions, *Phys. Earth Planet. Inter.*, *120*, 145–152.
Walte, N. P., J. K. Becker, P. D. Bons, D. C. Rubie, and D. J. Frost (2007), Liquid-distribution and attainment of textural equilibrium in a partially-molten crystalline system with a high-dihedral-angle liquid phase, *Earth Planet. Sci. Lett.*, *262*(3-4), 517–532.
Walte, N. P., D. C. Rubie, P. D. Bons, and D. J. Frost (2011), Deformation of a crystalline aggregate with a small percentage of high-dihedral-angle liquid; implications for core-mantle differentiation during planetary formation, *Earth Planet. Sci. Lett.*, *305*, 1–2.
Watters, W. A., M. T. Zuber, and B. H. Hager (2009), Thermal perturbations caused by large impacts and consequences for mantle convection, *J. Geophys. Res.*, *114*, E02001, doi:10.1029/2007JE002964.
Weinberg, R. F., and Y. Podladchikov (1994), Diapiric ascent of magmas through power law crust and mantle, *J. Geophys. Res.*, *99*, 9543–9559, doi:10.1029/93JB03461.
Wilhelms, D. E., and S. W. Squyres (1984), The Martian hemispheric dichotomy may be due to a giant impact, *Nature*, *309*, 138–140, doi:10.1038/309138a0.

Yiantsios, S. G., and R. H. Davis (1990), On the buoyancy-driven motion of a drop towards a rigid surface or a deformable interface, *J. Fluid Mech.*, *217*, 547–573, doi:10.1017/S0022112090000842.

Yoder, C. F., A. S. Konopliv, D. N. Yuan, E. M. Standish, and W. M. Folkner (2003), Fluid core size of Mars from detection of the solar tide, *Science*, *300*, 299–303, doi:10.1126/science.1079645.

Yoshino, T., M. J. Walter, and T. Katsura (2003), Core formation in planetesimals triggered by permeable flow, *Nature*, *422*, 154–157.

Zhong, S. J., and M. T. Zuber (2001), Degree-1 mantle convection and the crustal dichotomy on Mars, *Earth Planet. Sci. Lett.*, *189*, 75–84.

Ziethe, R., and T. Spohn (2007), Two-dimensional stokes flow around a heated cylinder: A possible application for diapirs in the mantle, *J. Geophys. Res.*, *112*, *B09403*, doi:10.1029/2006JB004789.